

Oxygen-dependent interactions between the ruthenium cage and the photoreleased inhibitor in NAMPT-targeted photoactivated chemotherapy

Selda Abyar^{1,2}, Lujiao Huang², Yurii Husiev¹, Ludovic Bretin¹, Bobby Chau^{1,2}, Vadde Ramu¹, Jaap Wildeman², Kimberley Belfor², Lukas Wijaya², V.E. van der Noord², Amy C. Harms², Maxime A. Siegler³, Sylvia E. Le Dévédec^{2,✉}, Sylvestre Bonnet^{1,✉}

¹ Leiden Institute of Chemistry, Leiden University, Gorlaeus Laboratories, PO Box 9502, 2300 RA Leiden (The Netherlands)

² Leiden Academic Centre for Drug Research, Leiden University, Gorlaeus Laboratories, PO Box 9502, 2300 RA Leiden (The Netherlands)

³ Department of Chemistry, Johns Hopkins University, 3400 N Charles St., Baltimore, MD, 21218 (USA)

✉ Corresponding authors email: s.e.ledevedec@lacdr.leidenuniv.nl, bonnet@chem.leidenuniv.nl

ABSTRACT

Photoactivated chemotherapy agents show a promising ability to kill cancer cells under the action of light, including those in chronic hypoxic conditions. Those compounds form a new branch of physically targeted anticancer agents with potentially lower systemic side effects for patients. On the other hand, very few information exists on the intracellular interactions between the photoreleased ruthenium cage and the photoreleased anticancer inhibitor. In this work, we report a biological study of the photoactivated chemotherapy compound **Ru-STF31** in the glioblastoma cancer cell line U87MG. **Ru-STF31** targets nicotinamide phosphoribosyltransferase (NAMPT), an enzyme overexpressed in glioblastoma. **Ru-STF31** is activated by red-light irradiation, which breaks a bond between the ruthenium-based caging group and the NAMPT inhibitor **STF31**, thereby releasing two photoproducts: the ruthenium cage and the cytotoxic inhibitor **STF31**. **Ru-STF31** showed significantly higher solubility in water and anticancer efficacy compared with the free inhibitor **STF-31**. It also significantly decreased intracellular NAD⁺ levels not only in normoxic (21% O₂) but also in hypoxic (1% O₂) U87MG cells. Strikingly, NAD⁺ depletion by red light activation of **Ru-STF31** in hypoxic U87MG cells could not be rescued by the addition of extracellular NAD⁺. Our data suggest an active role of the ruthenium photocage released by light activation.

INTRODUCTION

According to Global Cancer Statics (CNS), 308,102 new cases of brain and central nervous system (CNS) cancers were diagnosed in 2020 and 251,329 cancer-related deaths occurred in the same year¹. Gliomas represent 40% of all brain tumors, which makes them the most common and deadly human primary brain tumors. About half of all newly diagnosed gliomas correspond to glioblastoma (GBM), which is the most malignant type of brain cancer (grade IV) with a median overall survival of approximately 14–17 months in current clinical trials^{2 3} and around 12 months in population-based studies.^{1 3 4} Because of the heterogeneous nature of GBM, its treatment includes maximally safe surgical resection with subsequently parallel chemotherapy (Temozolomide) and fractionated radiotherapy.⁵ Consistently low tumor oxygenation (<1% O₂), also known as “chronic hypoxia”, is the main concern for GBM patients since it promotes cancer cells spreading into healthy brain tissues to evade the adverse hypoxic microenvironment.⁶ Although resection can achieve a reduction of the primary tumor burden, the observation that more than 80% of the recurrences are situated adjacent to the resection cavity suggests some utility for therapeutic platforms targeting this region.⁷ Previously, it has been shown that due to the weakly differentiated neoplastic astrocytes that do not release factors vital for the brain-blood barrier (BBB) function, leaky inter-endothelial tight junctions exist in human glioma. It was also demonstrated that BBB stability in lower-grade gliomas is better than that in GBM.⁸ As the degree of BBB disruption differs with the malignancy of the tumor, treatment of low-grade brain tumors is still a challenging task, because of the presence of almost intact BBB.⁹ Recently, the United States Food and Drug Administration (FDA) approval of 5-aminolevulinic acid (5-ALA) for fluorescence-guided resection (FGR) of tumors rehabilitated interests in leveraging this agent as a means to administer photodynamic therapy (PDT). PDT treatment to the tumor resection cavity can minimize the risk of local reappearance.¹⁰ PDT involves the photoactivation of a photosensitizer molecule called a photosensitizer, which is selectively incorporated into tumor cells. Light irradiation activates the photosensitizer by transferring energy from the light beam to the sensitizer, resulting after spin flip in the formation of a

photosensitizer triplet excited state. This excited state activates nearby dioxygen molecules to produce a massive dose of reactive oxygen species (ROS) that induce cell death.¹¹

Though PDT has demonstrated added value for the treatment of GMB patients,¹² and different forms of PDT are clinically approved for the treatment of tumors such as Barrett's esophagus or non-melanoma skin cancer, it has also some limits, including a reduced efficacy in the hypoxic regions of a tumor.¹³ For instance, few studies showed resistance of GBM to PDT when employed in the resection cavity using a cylindrical diffuser fibre after implanting it into the tumor.^{13,14,15} Another family of molecules called photoactivated chemotherapy (PACT) agents also makes use of visible light irradiation to generate high but localized doses of cytotoxic species, leading to lower systemic side effects *in vivo*.¹⁶ Unlike PDT, PACT activates the prodrug via an O₂-independent mechanism, including ligand photosubstitution,¹⁷ covalent bond photocleavage,¹⁸ or photoisomerization.¹⁹ Such activation modes lead to changes in the formula of the compound that induces biological damage to irradiated cells, for example by inhibiting an essential metabolic enzyme. Due to their O₂-independent mode of activation, a deficiency of dioxygen in the cancer cell does not necessarily affect the activation of PACT compounds, as demonstrated previously.^{20,21} Photocleavable groups based on ruthenium (Ru) are among the most pre-clinically promising photocages for PACT. While including a second-row transition metal²², these prodrugs often show less systemic toxicity than conventional antineoplastic agents based on e.g. platinum.²³ In addition, their photochemistry is well-understood and finely tunable (Lameijer et al., 2017). Although new PACT compounds, such as ruthenium-peptide conjugates,²⁴ show (photo-)toxicity in hypoxic tumor cells and multicellular tumor spheroids (MCTS), PACT has not been applied in the clinic yet.

In principle, ruthenium-based PACT compounds can be used to combat several hallmarks of cancer including uncontrolled proliferation and altered metabolism. Due to their high proliferation rate, cancer cells require a high amount of essential metabolites adenosine triphosphate (ATP) and nicotinamide adenine dinucleotide (NAD⁺). NAD⁺ and its reduced analogue NADH are very important electron carriers in cells. Both molecules allow cells to maintain good cellular homeostasis by acting as a substrate for PARP, mono/poly-ADP-ribosylation and Sirtuin-activated

ns deacetylation enzymes.²⁵ The regulation of NAD⁺ biosynthesis and transport as well as of that of its intermediates, is crucial to sustaining tumor cell growth.²⁶ NAD⁺ can be synthesized from various dietary precursor molecules via multiple pathways, but in cancer, NAD⁺ is predominantly produced via the so-called "salvage pathway".²⁷ Since cancer cells require a high amount of NAD⁺ to maintain their functions, multiple researchers have developed therapeutic strategies based on small molecule inhibitors such as FK866 or CHS-828.²⁸ These compounds prevent the formation of NAD⁺ by inhibiting nicotinamide phosphoribosyltransferase (NAMPT), an enzyme critical to the NAD⁺ salvage pathway. NAMPT, also called pre-B-cell colony-enhancing factor 1 (PBEF1) or visfatin, is a rate-limiting enzyme for NAD⁺ synthesis that plays an important role in tumor generation and progression.^{29,30} NAMPT is also described as a soluble factor with a cytokine-like activity that regulates cell growth, migration, and gene expression.³¹ Although NAMPT is a promising anti-cancer drug target, its targeting in patients offers a low therapeutic window, with either a lack of antitumor efficacy at lower doses or too many side effects at higher doses, such as retinal, hematological, or cardiac toxicity.³²

To solve this problem, the novel NAMPT-targeted PACT compound [Ru(tpy)(biq)(STF31)]Cl₂ (**Ru-STF31**, tpy = 2,2',6',2''-terpyridine; biq = 2,2'-biquinoline; STF31 = 4-[(4-(2-methyl-2-propanyl)phenyl)sulfonyl]amino)methyl]-N-(3-

pyridinyl)benzamide) has been recently proposed.²⁰ Upon red light irradiation (630 nm), **Ru-STF31** releases both **STF31** and the activated photocage **RuOH₂** (Figure 1, top). **STF31** is a commercially available cytotoxic NAMPT inhibitor that was also shown to influence the glucose transporter GLUT1.³³ It contains a metal-binding pyridyl group that allows blocking its NAMPT-inhibiting properties by coordination to the ruthenium-based photocaging group. **Ru-STF31** was demonstrated to become 2-4 times more cytotoxic upon red light activation *in vitro* in human lung (A549) and non-melanoma skin (A431) cancer cells, both in normoxia (21% O₂) and hypoxia (1% O₂)²⁰. Its activity in glioblastoma cells was, up to now, unknown. In addition, though the photocage is traditionally believed to play a minor role in the light-triggered activity of ruthenium-based PACT compounds, recent works have shown that this assumption may turn wrong.^{34,35} In principle, the biological activity of a PACT compound following light irradiation might, in fact, be a combination of the effect of the released inhibitor and of that of the photocage. In view of the low amount of information currently available on this question, we address it in detail here in the context of glioblastoma. We included in the study the analogue compound [Ru(tpy)(biq)(py)]Cl₂ (**Ru-Py**, Figure 1), a photoactivated ruthenium cage control that releases the same activated cage **RuOH₂** as **Ru-STF31**, together with the biologically benign pyridine, but not NAMPT inhibitor (Figure 1, bottom). We first compared NAMPT expression in different cell lines to demonstrate its overexpression in glioblastoma. Second, we measured separately the biological effects of **Ru-STF31** and **Ru-Py** after red light activation, and checked how the **STF31** inhibitor may interact biologically speaking, with the activated cage **RuOH₂**. Finally, we compared the antiproliferative effects of these compounds with their ability to modify the NAD⁺ levels in cancer cells using metabolomics, both in a normoxic and hypoxic context, which concluded to a non-negligible influence of the ruthenium caging group on the activity of the photoreleased **STF31** inhibitor, in particular under hypoxia.

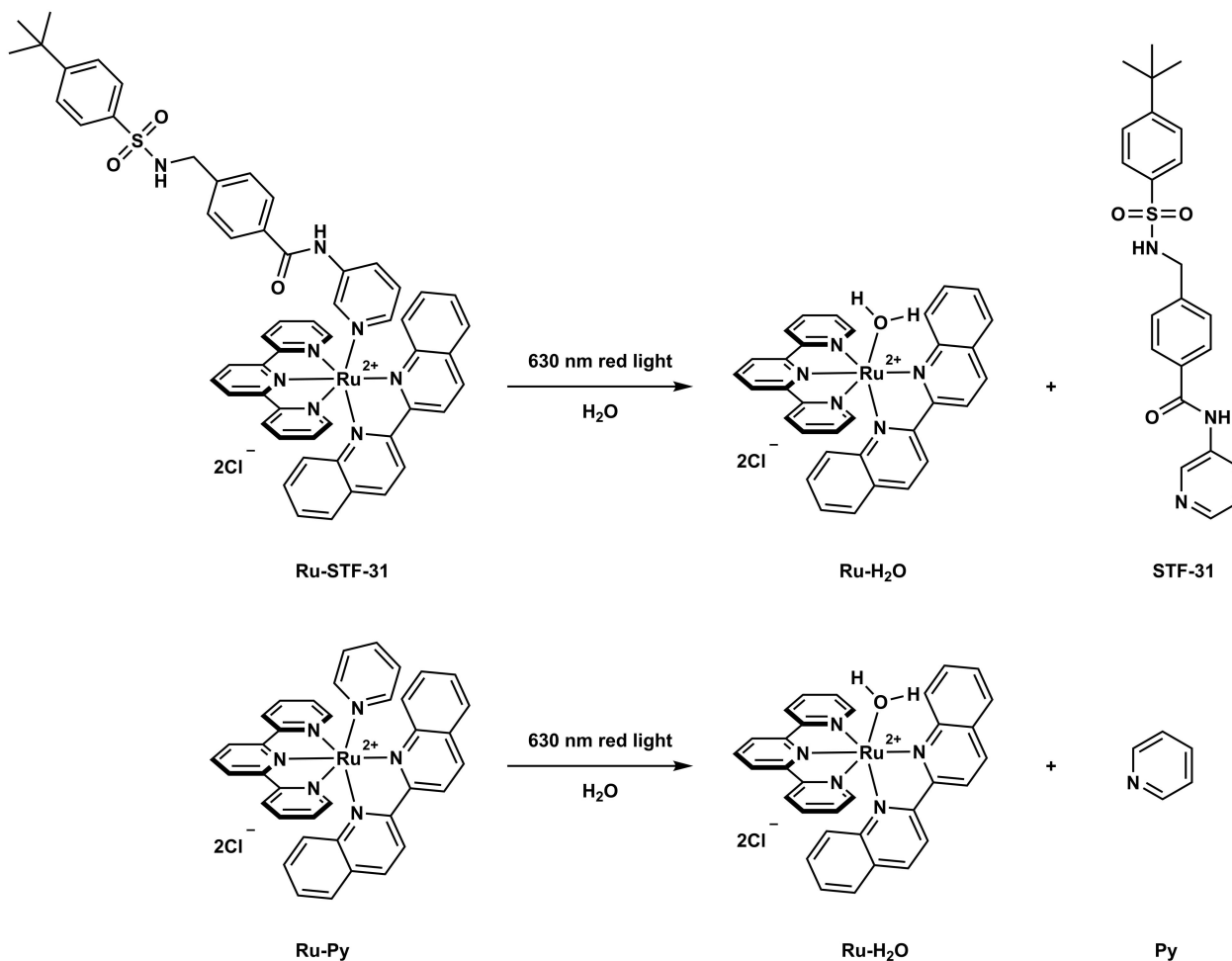


Figure 1. Light activation of the PACT compounds **Ru-STF-31** (top) and **Ru-Py** (bottom) by red light. Upon light absorption, both **Ru-STF-31** and **Ru-Py** release the activated photocage **RuOH₂**, but the former releases the NAMPT inhibitor **STF-31**, while the latter releases non-toxic pyridine (**Py**).

RESULT AND DISCUSSION

Crystal structure of Ru-STF31. As the experimental structure of **Ru-STF31** was unknown, single crystals of [Ru(tpy)(biq)(STF31)](BF₄)₂ were obtained by dissolving **Ru-STF31** in MeOH, adding a few drops of the HBF₄ diethylether complex, and waiting for crystallization to occur. Single crystals were obtained that allowed crystal structure determination. Due to the steric hindrance between the pyridyl group of **STF31** and the bisquinoline fragment, the biq ligand in the resulting structure was tilted, thus generating two enantiomers in the resolved crystal structure. One of them is shown in Figure 2. Selected bond distances, angles and other details are presented in Table S1-2 of supplementary information. This structure unequivocally demonstrates the binding of **STF31** via pyridine to the ruthenium center in the photocaged prodrug **Ru-STF31**.

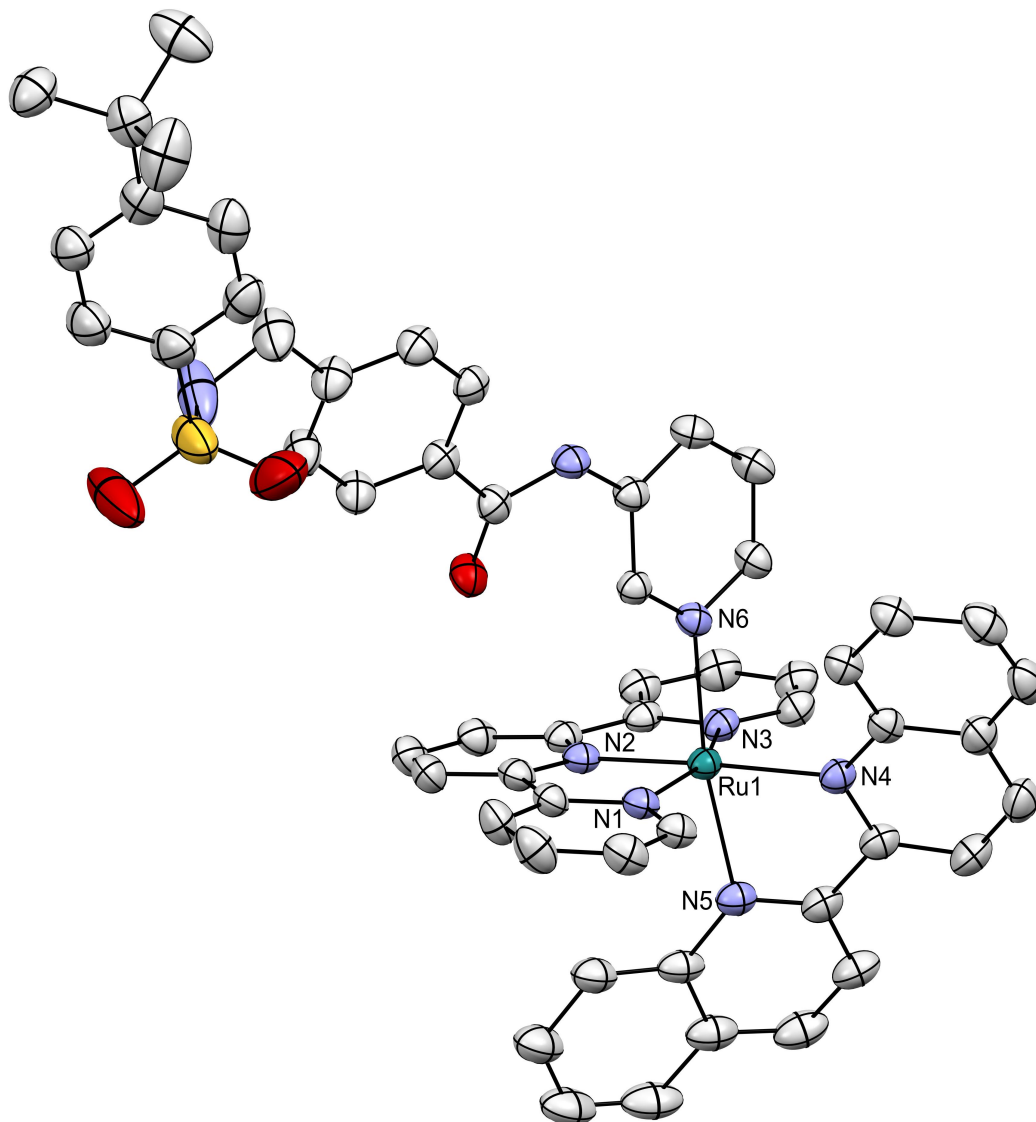


Figure 2. Displacement ellipsoid plot (50% probability level) of the crystal structure of the tetrafluoroborate salt of **Ru-STF-31** at 110(2) K. All hydrogen atoms and counterions have been omitted for clarity.

U87MG is the most suitable cell line for assessing the efficacy of Ru-caged NAMPT inhibitor. NAMPT overexpression was repeatedly reported in many human malignant tumors.³⁶ Figure 2A shows a box plot of pathology data extracted and selected from the Human protein atlas (Human Protein Atlas.org, version 22ith with considering RNA-seq data from Cancer Genome Atlas (TCGA)). We chose to highlight 5 out of 17 cancer types with an median expression level of 32.6 FPKM in our study (fragments per kilobase of exon per million mapped fragments). According to this analysis, glioma [n=153] turned out as the cancer type with the highest expression of NAMPT at the mRNA level. By contrast, with a median of 4.8 FPKM endometrial cancer was found as the cancer having the lowest expression of NAMPT [n=541]. To validate this clinical observation *in vitro*, we measured NAMPT protein levels by western blot in

a selection of 5 cell lines representative of different cancer including non-melanoma skin (A431), liver (HEPG2), lung (A549), skin melanoma (A375), and glioblastoma (U87MG). These measurements were performed at two O₂ concentrations, 21% (hereafter called normoxia) and 1% (hereafter called hypoxia), to assess the influence of oxygen concentration on NAMPT expression. As shown in Figure 2C, within these 5 cancer cells lines U87MG displayed the highest level of NAMPT protein, independently from the oxygen level. Supposedly, U87MG mostly produces NAD⁺ via the salvage pathway, and hence need a higher expression of NAMPT as it is a crucial enzyme in this pathway (Sharma et al., 2021). Both HEPG2 and A431 cell lines were found to have the lowest NAMPT protein level of this series; the HEPG2 cell line was selected in further studies as NAMPT-negative, low expression control cell line.

In fact, U87MG cells showed high NAMPT expression at both the mRNA and protein levels, but it is not the only brain cancer cell line. To investigate how U87MG expressed NAMPT within other known brain cancer cells lines, we plotted the NAMPT mRNA levels of a large compendium of 25 brain cancer cell lines retrieved from the Human Protein Atlas. Of the 25 brain cancer cell lines panel, we display in figure 2D the average value of NAMPT mRNA level of 25 cell lines with high, medium and low expression. Surprisingly, with a value of 362 nTPM (normalized transcripts per million) the U87MG cancer cell line expressed the highest NAMPT mRNA level of the whole series. In fact, NAMPT is not only highly expressed in glioblastoma cell lines, but it is also associated in the clinics with a worse prognosis for brain cancer patients: a high NAMPT protein level is associated with a higher grade of GBM. From the human protein atlas database, the differential NAMPT expression in high-grade and low-grade GBM from 2 different patients was retrieved (Figure 2E). The higher expression of NAMPT was observed in patients with highest-grade GBM, which may indicate a possible association between NAMPT levels and the aggressiveness of the disease. Finally, Figure 2F illustrates a Kaplan-Meier curve based on TCGA database analysis of 153 patients, indicating that higher NAMPT expression is associated with increased mortality among glioblastoma patients compared to those with lower NAMPT expression. Overall, NAMPT appeared clinically as a good target for NAMPT-targeted PACT drugs such as **Ru-STF31**, and U87MG cells was one of the best *in vitro* models tested to test the activity of this PACT agent.

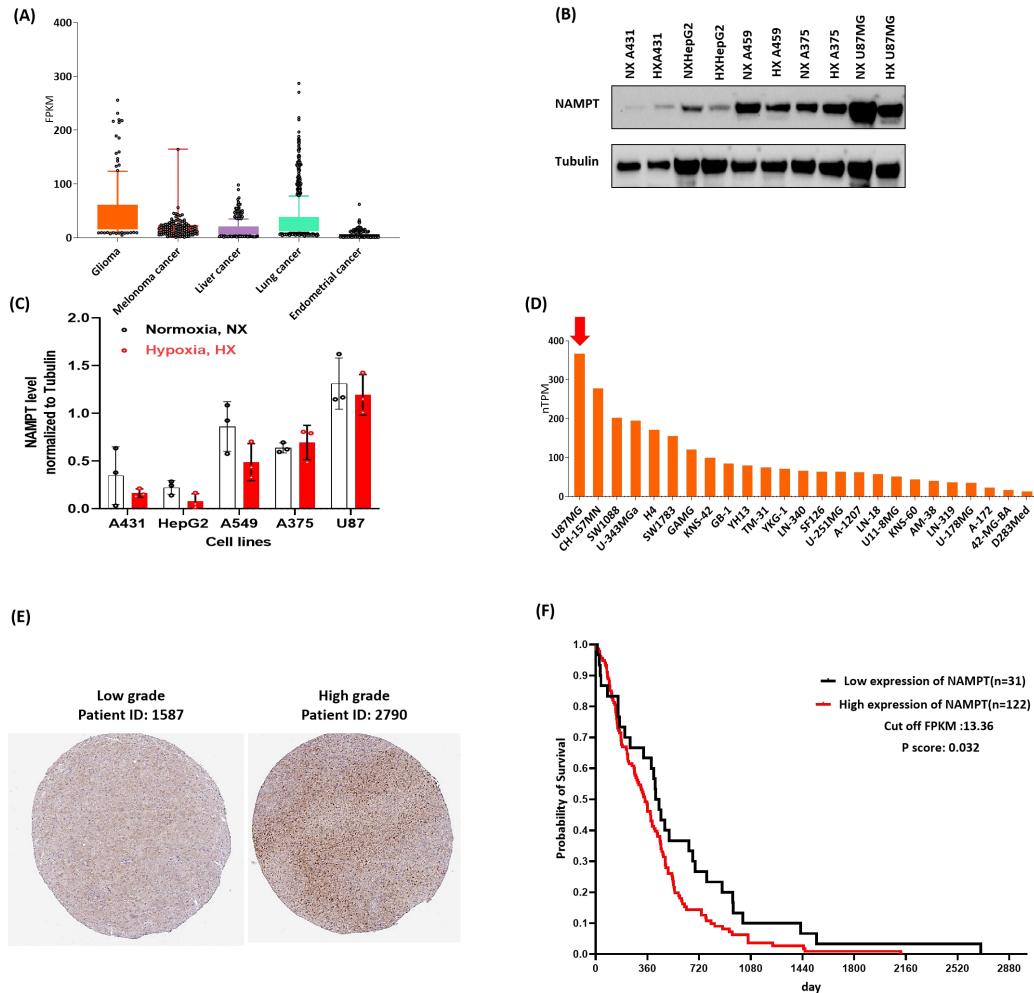


Figure 3. (A) NAMPT RNA-seq data for 5 cancers types from TCGA, were analyzed and reported as the median number of fragment per kilobase of exon per million reads(FPKM), reported as median FPKM (<https://www.proteinatlas.org/> version 22.0). Normal distribution across dataset was visualized by box plots, shown as median and 25th and 75th percentiles, Points are shown as outliers if they are above or below 1.5 times the interquartile range. (B) Western blotting of NAMPT expression among five different cancer cell lines cultured in both hypoxic (1% O₂) and normoxic (21% O₂) conditions showing highest and lowest NAMPT expression in U87MG and HEPG2, respectively (C) Bar-graph of the western blotting assay, each bar represents a value for the NAMPT protein, (D) Bar graph provided by the human protein atlas version 22.0 and ensemble version 103.38, showing the highest expressions of NAMPT in U87 MG among different brain cell lines [n=25] (E) Expression of NAMPT by HPA047776 antibody in brain tissue of patient with high grade (right tissue) and low grade (left tissue) GBM provided by human protein atlas (<https://www.proteinatlas.org/> version 22.0) showing relatively higher expression of NAMPT in high grade GBM. (F) A Kaplan-Meier curve was plotted for 153 GBM patients, stratified by high (n=122) and low (n=31) expression levels of NAMPT, using a cutoff of 13.62 FPKM for RNA expression.

Hypoxic phenotype in U87MG cells. To validate our hypoxic cell culture conditions, we first immunostained HIF1- α in both normoxic (21% O₂) and hypoxic (1% O₂) U87MG cells (Figure 3A). As a positive control, we treated normoxic cells with CoCl₂ (100 μ M), a chemical inducer of HIF-1 α protein stabilization.³⁷ As reported a low level of HIF1- α protein was observed in normoxic U87MG cells, which was increased upon treatment of the cells with CoCl₂ (Figure 3A). Furthermore, by incubating the U87MG cells for at least 10 days in hypoxic conditions (1% O₂), an comparable increased level of HIF1- α was also observed (Figure 3A). The merged images (Figure 3A, bottom) also showed the translocation of HIF1- α into the nucleus, indicated by white arrows. These results validated the stabilization of HIF1- α and its translocation to the nucleus in hypoxic U87MG cells, in response to low oxygen levels.

Second, we investigated the impact of HIF1- α nuclear colocalization on the hypoxic response in U87MG cells cultured in low oxygen conditions by conducting transcriptomics analysis (Figure 3B-3D). Our observations revealed a substantial upregulation not only of the direct target genes of the transcription factor HIF1- α , such as 2 isomer of CA9 (carbonic anhydrase 9) and one isomer of VEGFA (vascular endothelial growth factor), showing log₂fold changes of 4.78 and 8.45, respectively, but also in genes contributing to glycolysis, including GAPDH, ALDOA, ENO1&2, with log₂fold changes of 2.63, 1.76, and 3.13, 9.66, respectively (Fig 3B-3C). Altogether, these transcriptomics data supported our immunostaining imaging and concluded to the activation of the HIF1- α pathway in U87MG cells in hypoxic (1% O₂) conditions. Although NAMPT upregulation under hypoxia was not evident at the protein level (Figure 1B), transcriptomics data indicated an increase in NAMPT mRNA levels under low oxygen conditions in U87MG cells. Intriguingly, the analysis revealed a downregulation of numerous genes associated with the NAD⁺ salvage pathway like as SLC29A2, NAPRT in hypoxia (Fig. 3D). Overall, hypoxic U87MG cells appear as a more suitable *in vitro* model for testing **Ru-STF31**, notably compared to our previous study using A549 and A431 cells.²⁰

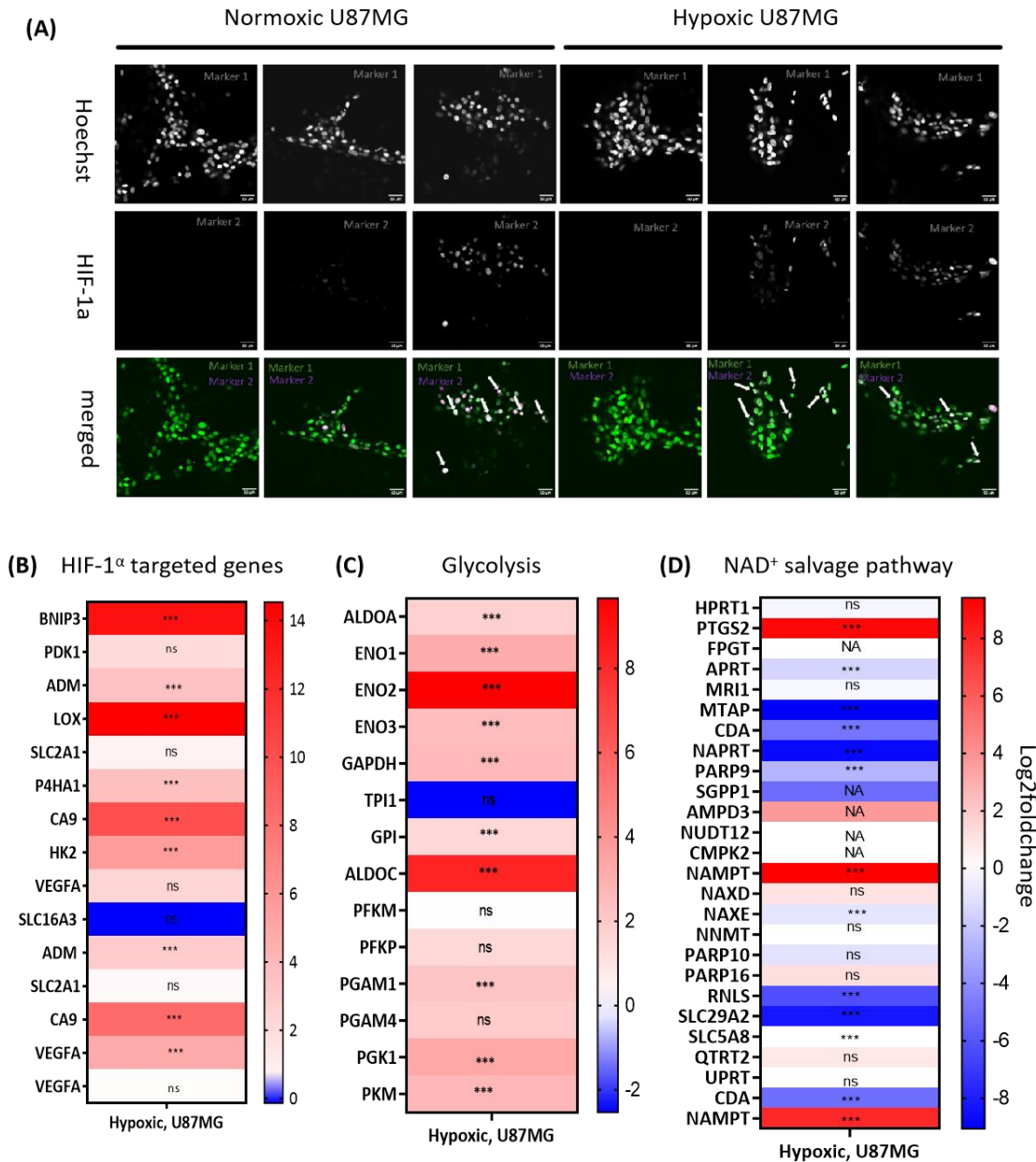


Figure 4. (A) Immunostaining of HIF1- α in U87MG cells cultured in normoxia (21% O₂) and hypoxia (1% O₂). Normoxic U87MG cells (left panel) and hypoxic U87MG cells (right panel) were imaged using confocal microscopy. Immunofluorescent staining of HIF1- α is shown in green (middle panel), cell nuclei are stained in blue with Hoechst dye (upper panel) and the merged images are shown in the bottom panel. The control (-) group represents cells with secondary and without primary HIF1- α staining (negative control). The (+) groups represents cells with both primary and secondary HIF1- α staining. Cells treated with CoCl₂ (100 μ M) for 24 h were included as positive control for the expression of HIF1- α . Overexpression and translocation of HIF-1 α were observed in both hypoxic U87MG cells and normoxic cells treated with CoCl₂. Heat map of differentially expressed (B) HIF-1 α targeted genes (C) Genes involved

in glycolysis, (D) Genes in NAD⁺ salvage pathway, . NA: not available values; significant p-values are indicated with ***, padj<0.01. ns: non-significant.

Cellular toxicity of Ru-STF31. Having identified U87MG as high NAMPT-expressing cell line and HEPG2 as low NAMPT-expressing cell line, we measured the cytotoxicity of the photoactivatable NAMPT inhibitor **Ru-STF31** both in the dark and following red light irradiation in both cell lines (Figure 4). Following exposure to red light irradiation (RL, 630 nm, 20.8 J/cm²), **Ru-STF31** exhibited increased toxicity with EC₅₀ values of 9.7 μM and 22.7 μM in normoxic and hypoxic U87MG cells, respectively, compared to dark conditions (27.8 μM and 35 μM, see Figure 4). The photoindex (PI) value of **Ru-STF31**, defined as EC₅₀(D)/EC₅₀(R), was approximately 2.86 and 1.53 respectively, in normoxic and hypoxic U87MG cells, indicating significantly enhanced cytotoxicity under red-light irradiation. Under normoxia lower cytotoxicity was observed for the free inhibitor **STF31** (EC₅₀ = 30 μM) in U87MG cells in comparison with that of red light-activated **Ru-STF31** (9.7 μM, Table 1). In HEPG2 cells the toxicity of **Ru-STF31** under red light conditions (EC₅₀ = 15 μM and 30.8 μM, respectively) was slightly lower than that in U87MG cells. No significant PI values were observed for **Ru-STF31** in normoxic (1.73) and hypoxic HEPG2 cells (1.1).

To investigate the biological effect of the **RuOH₂** cage alone, we also tested the cytotoxicity of **Ru-Py** in the same conditions. Interestingly, cell viability indicated that **Ru-Py** like **Ru-STF31** showed light-dependent cytotoxicity, both under normoxic and hypoxic conditions (Table 1 and Figure 5). Clearly, although the phototoxicity and dark toxicity of **Ru-Py** was lower than that of **Ru-STF31** in both normoxic and hypoxic U87MG cells, the ruthenium photocage showed a biological activity upon light activation that had been overlooked before. In addition, the EC_{50,RL} values of **Ru-Py** were 32.9 and 44.9 μM under normoxia and hypoxia, respectively, which was higher than that of **Ru-STF31** in the same conditions. Overall, according to these results light-activated **Ru-STF31** had lower EC₅₀ value, both under normoxia and hypoxia, than free **STF31** and light-activated **Ru-Py**, which suggested that both photoreleased fragments **STF31** and **RuOH₂** (Figure 1) might exert a synergistic cytotoxic (or cytostatic) action.

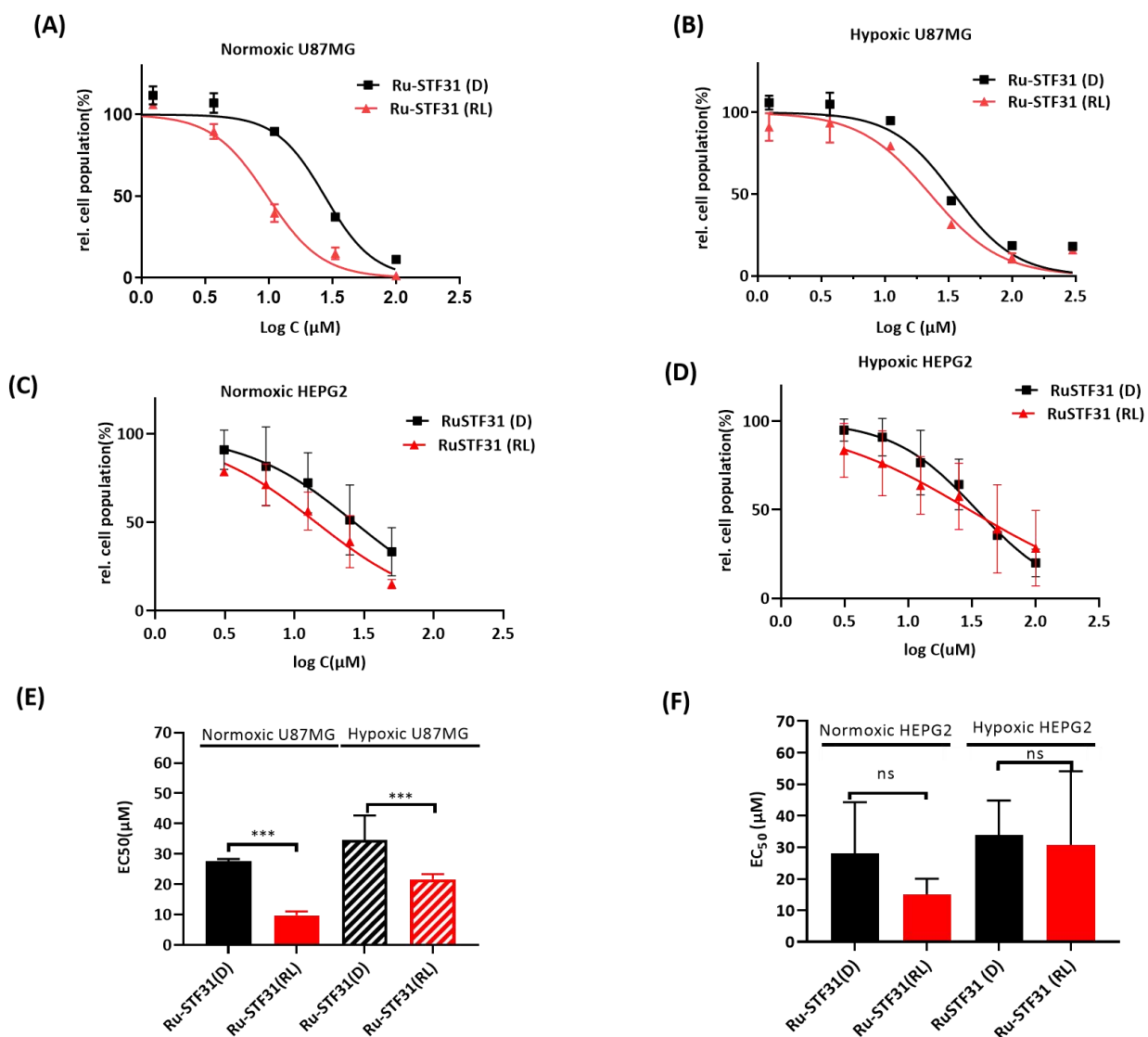


Figure 5. Dose-response curves of **Ru-STF31** for (A) normoxic U87MG cells; (B) hypoxic U87MG cells; (C) normoxic HEPG2 cells; (D) or hypoxic HEPG2 cells. All cells were treated with **Ru-STF31** and kept in the dark (black data points) or irradiated by red light (630 nm, 20.8 J/cm², red data points). Data points are averages of three biological replicates (n=3) with 95 % confidence intervals (in μM). (E) and (F): corresponding bar graphs showing cell viability of **Ru-STF31** (D& RL) in U87MG and HEPG2 cells, respectively. Statistical significance was assessed via one-way ANOVA test, **p<0.05, *** ≤0.01, **** ≤0.001.

Table 1. EC₅₀ values of **Ru-STF31** (D, RL), **Ru-Py** (D, RL), and **STF-31** in normoxic and hypoxic U87MG human glioblastoma cells.

Compound	Parameters	Conditions	
		Normoxia (21%O ₂)	Hypoxia (1%O ₂)
STF31	EC ₅₀ (D), μM	30.2	130
	95%CI, μM	+15.3/-9.50	+86.7/-43.8
	EC ₅₀ (RL), μM	-	-
	95%CI, μM	-	-
Ru-Py	EC ₅₀ (D), μM	124	133
	95%CI, μM	+31.2/-23.6	+29.8/-23.9
	EC ₅₀ (RL), μM	32.9	44.9
	95%CI, μM	+10.5/-7.58	+22.6/-14.1
Ru-STF31	EC ₅₀ (D), μM	27.8	35.0
	95%CI, μM	+5.91/-4.83	+12.5/-8.35
	EC ₅₀ (RL), μM	9.7	22.7
	95%CI, μM	+1.56/-1.29	+7.35/-5.45

Impact of red light-activated Ru-Py on the cytotoxicity of STF31. Considering the biological activity of **Ru-Py** upon red light activation, one could wonder whether the ruthenium photocage after light activation of **Ru-STF31** interacts with the photo-released **STF31** inhibitor. To address this question, we investigated the cytotoxicity of a combination of red light-activated **Ru-Py** and free **STF31**, both under normoxia and hypoxia (Figure 6). The combination index (CI) values were computed based on Chou-Talalay method³⁸ using the CompuSyn software (www.combosyn.com). This method is based on the median-effect equation (MEE) of the mass-action law (MAL) expressed in Equation 1:

$$\frac{F_a}{F_u} = \left(\frac{D}{D_m}\right)^m \quad (1)$$

where F_a is the fraction affected by the drug (here, cell growth inhibition) and F_u is the fraction unaffected by the drug, D is the dose of the drug, D_m is the median-effect dose or potency of the drug, and m is the slope of the dose-response S-shaped curve. In this formalism the CI values for each combination and each resulting effect F_a can be calculated by Equation 2:

$$CI = \frac{(D_{Ru-Py(RL),mix})_{F_a}}{(D_{Ru-Py(RL)})_{F_a}} + \frac{(D_{STF31,mix})_{F_a}}{(D_{STF31})_{F_a}} \quad (2)$$

Where $(D_{x,mix})_{F_a}$ represent the concentration (in μM) of drug x in the combination to achieve a specific effect, and $(D_x)_{F_a}$ represents the concentration (in μM) of drug x taken alone to achieve the same effect F_a as the combination. The CI provides information about the effect of the combination, compared with an additive effect. CI values lower than 1 indicate synergism, CI = 1 indicates additive effects, and CI values higher than 1 indicate antagonism. All details and the CompuSyn report of **Ru-Py** (RL) and STF31 including media effect plot are given in the Supplementary Information (Figure S19).

Strikingly, different CI values were found under normoxia and hypoxia. Under normoxia, at the highest concentrations used where both compounds individually achieved a 75 and 85% effect (F_a) on cell death (Figure 6B), CI values lower than 1 were found, corresponding to synergies. However, at lower concentrations an unexpected antagonistic effect was observed with

CI values either close to 1 or clearly higher than 1. In contrast, in hypoxic (HX) cells a consistent synergy pattern emerged from the data irrespective of the drug concentrations, with all CI values lower than 1 in a 1:1 mixture of **Ru-Py**(RL) and free **STF31**.³⁹ Hence, in hypoxic U87MG cells the photoreleased ruthenium cage **RuOH₂** was found to exert a synergistic influence on the effect of the **STF31** inhibitor itself. To our knowledge, this observation is the first report on the one hand of the fact that the ruthenium cage may influence the biological effects of the photoreleased inhibitor (here **STF31**). On the other hand, these interactions were found dependent on the oxygenation level of the cells.

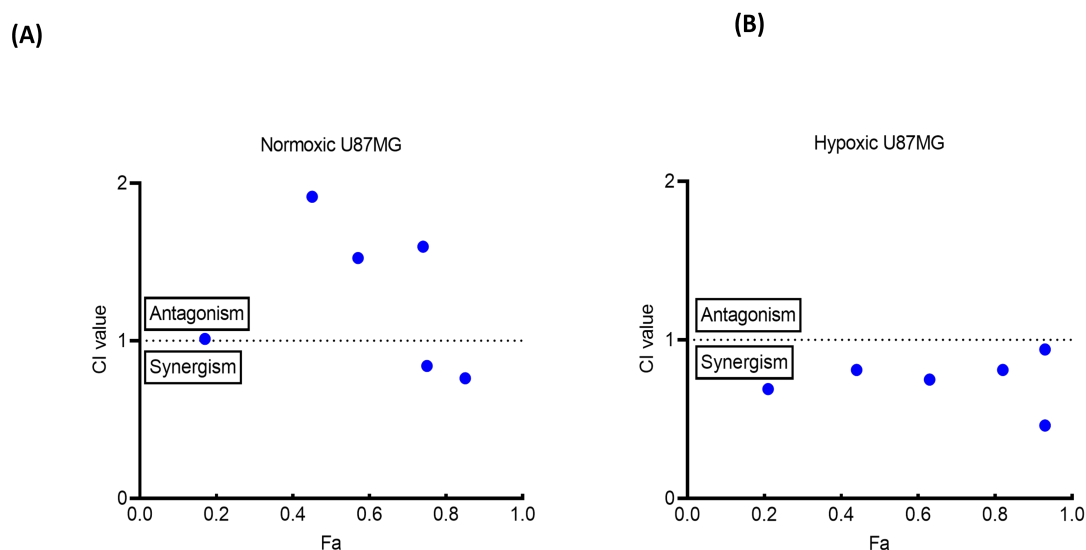


Figure 6. Combination index plot for combination therapy of **Ru-Py**(RL) and **STF31**, in 1:1 concentration ratio in both (A) normoxic (21% O₂) and (B) hypoxic (1% O₂) U87MG cells. The X-axis represent the fraction affected by the drug (f_a) while the Y-axis shows the combination index value at each value of F_a .

Reduction of intracellular NAD⁺ level in hypoxic (HX) U87MG cells treated with **Ru-STF31**.

Based on the cell-free NAMPT enzyme activity assay used in our previous report,²⁰ we expected that NAMPT inhibition with light-activated **Ru-STF31** would reduce the intracellular levels of NAD⁺. However, this hypothesis had never been tested in a cellular context. Therefore, we conducted a metabolomic analysis to measure the real intracellular level of NAD⁺ in U87MG cells cultured in different conditions: either untreated (Ctrl) or treated with **Ru-STF31**, **Ru-Py**, or **STF31**, and either kept in the dark (D) or following activation with red light (RL, 20.8 J/cm²).^{40 41} According to this analysis, free **STF31** significantly decreased NAD⁺ levels in hypoxic cells but the change compared with untreated cells was not statistically significant in normoxic cells. In normoxia, **Ru-STF31** in both dark and red light-activated conditions, did not affect the amount of NAD⁺; however, in hypoxic cells light-activated **Ru-STF31** significantly decreased NAD⁺ levels. This observation was consistent with our findings regarding the free inhibitor **STF31**, indicating that treatment with the free NAMPT inhibitor or with its light-activated analogue **Ru-STF31** did lead to a reduction in NAD⁺ levels in U87MG cells, but only in hypoxic conditions.

Of course, **Ru-Py** was originally designed as a negative control for NAMPT inhibition. Consequently, it was expected not to have any effect on intracellular NAD⁺ levels. This usual assumption appeared to be correct for normoxic U87MG cells, where **Ru-Py**, whether light-

activated or not, did not induce statistically significant differences of the NAD^+ levels with respect to untreated cells. However, it appeared as incorrect in hypoxic U87MG cells: **Ru-Py** before activation by red light did increase NAD^+ , and following red-light activation and release of **RuOH₂**, unexpectedly decreased intracellular NAD^+ levels. Although it was unclear, at this stage, if **Ru-Py** had any NAMPT inhibitory effect, in hypoxic cells the ruthenium cage was found to increase NAD^+ level whether activated or not. Maybe as a defense mechanism against the toxicity of **Ru-Py**, which seems to disturb cellular hemostasis (Okabe et al., 2019).

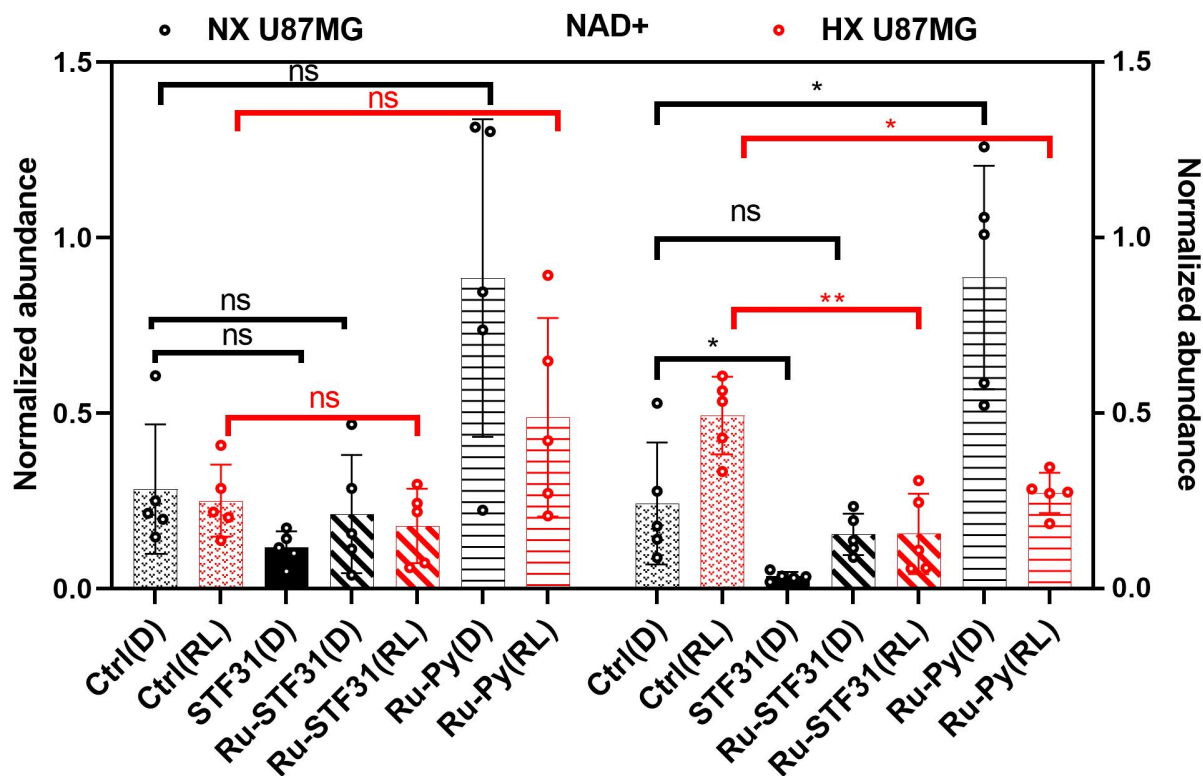


Figure 7. Metabolomics analysis of NAD^+ level in U87MG cells treated with vehicle control (Ctrl), STF31, Ru-STF31, or Ru-Py, and kept in the dark (D) or irradiated with red light (RL, 630 nm, 20.8 J/cm²). Data points are averages of 5 biologically independent experiments (n=5) and error bars represent 95 % confidence intervals. Statistics: paired student t-test, p-value: 0.1234 (ns), 0.0332 (*), 0.0021 (**), 0.0002 (***).

Rescue experiments of STF31 and Ru-STF31 with NAD^+ . In principle, decreasing the intracellular levels of NAD^+ in U87MG cells by NAMPT inhibitors may be effective and harm the cells if no extracellular NAD^+ can be taken up by the cancer cells. However, *in vivo* the tumor microenvironment has the potential to provide critical metabolites like NAD^+ to promote tumor growth. Therefore, we decided to investigate if adding NAD^+ in the culture medium of hypoxic U87MG cells treated with red light-activated Ru-STF31 or STF31 would rescue them or not, hence lower toxicity of the inhibitor. To this aim, three different ratios between the ruthenium drug and NAD^+ were investigated, ie 1:1, 1:7.5 and 1:15. For instance, for the 1:1 ratio hypoxic U87MG cells were treated with Ru-STF31 or STF31 in a concentration range 100-3.1 μM . Following photoactivation of Ru-STF31, which released STF31, or in the dark for STF31, NAD^+ was added to the cells at the same concentration as the drug (concentration range 100-

3.1 μM). For free **STF31**, the toxicity of the drug towards U87MG cells was as expected reduced at all drug: NAD^+ ratios (Figure 8B). This result supported the hypothesis that the presence of additional NAD^+ in the culture medium “rescued” the toxic effects of the NAMPT inhibitor **STF31**. In other words, free **STF31** and NAD^+ acted antagonistically for cell killing. For light-activated **Ru-STF31**, however, a reverse effect was obtained, i.e., the EC_{50} value of the ruthenium PACT compound after red light activation was decreased when the treatment was combined with various concentration ratios of NAD^+ (1:1, 1:7.5, or 1:15, see Figure 8A). This unexpected result suggested that a synergistic effect occurred, in toxicity terms, when red light-activated **Ru-STF31** was combined with NAD^+ . In conclusion, in hypoxic U87MG cells the toxicity resulting from red light-activated **Ru-STF31** could not be rescued by adding additional NAD^+ . On the contrary, synergistic cytotoxic effects were observed at all ratios of the combined treatment, suggesting that extracellular NAD^+ provided by the tumor microenvironment may even increase the effect of the PACT prodrug in hypoxic regions after light activation. Though it is unclear, at this stage, where this phenomenon comes from, our data clearly highlight that the simple picture of a light-activated inhibitors targeted to NAMPT is, in fact, more complicated than initially expected.

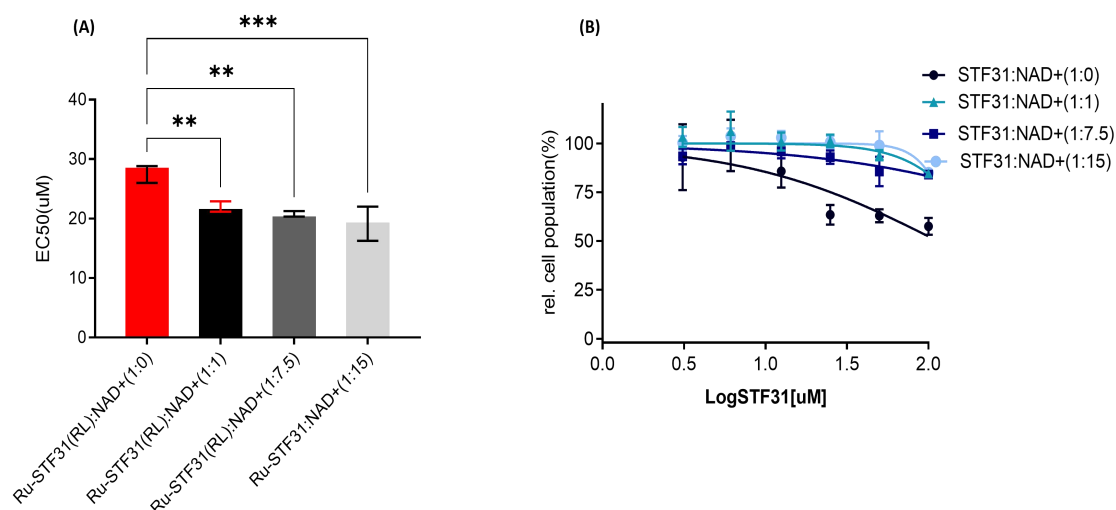


Figure 8. Combination treatment of extracellular NAD^+ with (A) **Ru-STF31** activated by red light (630 nm, 20.8 J/cm²), or (B) **STF31** in hypoxic U87MG cells. Both drugs were introduced in a concentration range 100-3.1 μM , and NAD^+ was introduced in 4 concentration ratios with the drug, i.e., **Ru-STF31**: NAD^+ or **STF31**: NAD^+ were 1:0, 1:1, 1:7.5, or 1:15. Statistical significance was assessed through ordinary one-way ANOVA, **= $p \leq 0.05$, *** ≤ 0.01 , *** ≤ 0.001 .

General discussion

In our study, it first appeared that U87MG glioblastoma cells serve as a highly appealing *in vitro* model for testing photoactivated NAMPT inhibitors such as **Ru-STF31**. Our results suggested that the correlation between NAMPT expression and glioma grading aligned with previous studies^{42,43} and supported the idea that NAMPT may play a role in glioma aggressiveness and progression. This insight also highlighted that NAMPT-targeted light-activated therapies are promising strategies to manage high-grade gliomas more effectively. Moreover, we showed that when culturing U87MG cells in hypoxic conditions (1% O_2) for at least 10 days, stabilization of

HIF-1 α and nuclear translocation occurs, leading to substantial upregulation of genes associated with the HIF1- α pathway. Hypoxic U87MG cells may hence represent a good *in vitro* model for hypoxic regions of glioma tumors. Following this hypothesis, we assessed the impact of NAMPT expression levels on the efficacy of the photoactivated NAMPT inhibitor **Ru-STF31** using U87MG cells as a model of cell line with high NAMPT expression, and HEPG2 as control cell line with low NAMPT expression. Despite expecting higher toxicity in U87MG, we were aware of the potential development of resistance mechanisms in cells with elevated expression of the target protein,⁴⁴ or in cells with low O₂ concentrations.⁶ These adaptive responses could both diminish the effectiveness of **Ru-STF31**. We observed significantly increased toxicity of **Ru-STF31** in red-light conditions in U87MG (9.7 μ M) compared to HEPG2 (21.6 μ M), highlighting its more potent impact on high NAMPT-expressing cells while comparable toxicity was found in the dark in both cell lines. On paper, the expression level of NAMPT should be crucial for the effectiveness of **Ru-STF31** because it targets NAMPT following light activation: higher expression levels of NAMPT in U87MG cells should likely result in greater binding and inhibition by **Ru-STF31**, leading to increased cytotoxicity upon light activation. In addition, the absence of significant PI values in low NAMPT-expressing HEPG2 cells suggested that the absence of effectiveness for **Ru-STF31** in this cell line may be directly related to its low NAMPT expression level. According to these results, the biological results seemed to follow the design of the molecule.

On the other hand, we realized that the lower toxicity of our compound in hypoxic U87MG cell line compared to normoxic ones, did not follow the expected pattern. STF31 was also described as GLUT1 inhibitor, and we wondered whether the influence of O₂ on the activity of the activated drug under hypoxia may be attributed to other factors like differential glycolysis⁴⁵ which we observed in our transcriptomics analysis for glycolysis differentially express of genes like GAPDH, ALDOA, ENO1&2. These genes plays crucial role in glycolysis and could contributed to the observed changes in cellular toxicity of our compounds. These doubts prompted further study on the mechanisms underlying cell death in U87MG cells.

In fact, the observed patterns of synergy or antagonism in the combination study of red light-activated **Ru-Py** and free **STF31** in hypoxic and normoxic U87MG cells presents important insight on the effects of oxygen on the biological effects of PACT prodrugs. The synergy which was observed in hypoxia at a 1:1 concentration ratio, suggested that the presence of red-light activated **Ru-Py** (**RuOH2** in Figure 1) in hypoxic cells also containing free **SFT31**, enhanced the toxic effects of the organic NAMPT inhibitor. Such enhancement may possibly come from complementary mechanisms or pathways that are more pronounced under low oxygen levels. For instance, our metabolomics data indicate an unexpected decrease in NAD⁺ levels in hypoxia in the presence of light-activated **Ru-Py** that is quite similar to the NAD⁺-lowering effects of the free inhibitor **STF31** in the same conditions. Such effects of the ruthenium cage were certainly not expected when designing **Ru-STF31**, but they fit well with the observed synergistic cytotoxicity between light-activated **Ru-Py** and free **STF31**. The significant reduction in NAD⁺ levels under hypoxia indicated a shared therapeutic effect of both fragments obtained after light activation of **Ru-STF31**, specifically in lowering intracellular NAD⁺ levels. Such decrease in NAD⁺ levels in a hypoxic microenvironment is noteworthy as NAD⁺ is a crucial coenzyme involved in various cellular processes. Overall, the observed synergy between **RuOH2** and **STF31** in reducing NAD⁺ levels could indicate a promising way for therapeutic mediation, particularly in hypoxic tumor regions where single treatments may be less effective.⁴⁶

On the other hand, the unexpected antagonistic effect observed at lower concentrations in normoxic U87MG cells, and the overall concentration-dependent synergies observed in our

combination study, indicated a more complex interaction between **RuOH₂** and **STF31** in an oxygen-rich environment. This second main result of our study suggested that the interplay between both photoreleased fragments of **Ru-STF31** following light irradiation may vary based on the cellular context. It also highlights the importance of seriously probing oxygen⁴⁷ levels in tumor tissues when designing combination therapies or PACT treatment with compounds such as **Ru-STF31**. Recent studies have reported that NAMPT inhibitors may synergize with DNA damage-inducing chemotherapeutics,³⁶ but these studies did not consider the potential influence of dioxygen. Usually, investigations on the synergies between different drugs focus on the molecular and cellular mechanisms targeted by these drugs. Our observations on the important role of O₂ in the activation of **Ru-STF31** may prompt a revision of existing combination therapies involving NAMPT inhibitors, urging researchers and clinicians to consider the oxygen status of a tumor as an additional environmental variable influencing drug-drug interactions or interactions between drug fragments – here those obtained by photochemical cleavage of the coordination bond between ruthenium and the NAMPT inhibitor **STF31**.

While **STF31** appears toxic to cells, according to metabolomics it did not significantly affect NAD⁺ levels in normoxic conditions, suggesting that its toxicity may be due to effects other than NAMPT inhibition. It is worth noting that **STF31** has been reported as an inhibitor of the glucose transporter1 (GLUT1).⁴⁸ GLUT1 inhibition by **STF31** and DNA methylation by temozolomide showed synergistic effects in glioblastoma.⁴⁹ Considering the known DNA-binding abilities of ruthenium complexes with open positions in their coordination sphere,⁵⁰ the higher PI value in normoxia might result from off-targets, such as GLUT1 inhibition and/or DNA binding of **RuOH₂**. In other terms, the phototoxicity of **Ru-STF31** under normoxia might be unrelated to NAMPT inhibition. Under hypoxia, GLUT1 overexpression might take place, rendering this mechanism irrelevant, while DNA damage may be modified by the different conditions, overall leading to lower phototoxicity after red light activation, and hence lower photoindex. In such conditions the selective reduction of NAD⁺ levels by **Ru-STF31** after light activation, may explain the remaining effect of the activated drug. Combining **Ru-STF31**(RL) with other drugs that act specifically in hypoxic conditions, such as autophagy inhibitors like chloroquine or hydroxychloroquine, holds promise for enhancing hypoxic cancer therapy. Overall, the unexpected effects of **Ru-Py** challenge our initial assumption that it would not impact NAD⁺ levels. The observed increase in NAD⁺ levels before activation and the subsequent decrease after activation by red light suggest complex cellular responses to simple ruthenium complexes such as **Ru-Py**. These responses may involve adaptive mechanisms or compensatory pathways.

Though synergies were identified by comparing one vs. mixtures of two drugs **RuOH₂** and **STF31** in hypoxic cells, which is usually interpreted as a good thing as it results in low EC_{50,RL} for light-activated **Ru-STF31**, one should not ignore the disappointingly low photoindex found for this compound under hypoxia (PI=1.5), which make it a not very successful light-activated drug in such conditions. Such low PI values must hence be re-interpreted as a consequence of a comparatively low EC_{50,D}, and hence a high toxicity for **Ru-STF31** in hypoxic dark conditions. Indeed, the EC_{50,D} of **STF31**, **Ru-Py**, and **Ru-STF31**, were 130, 44.9, and 35.0 μM, respectively, which highlighted that the “prodrug” **Ru-STF31** was, in the dark, much more cytotoxic than the free inhibitor **STF31**, and a bit more toxic than the non-activated ruthenium cage **Ru-Py**. In normoxia, the photoindex of **Ru-STF31** was significantly higher (2.9) than in hypoxia in spite of the absence of clear-cut synergies between **RuOH₂** and **STF31** after light activation, simply because the EC_{50,D} of free **STF31**, **Ru-Py**, and **Ru-STF31**, were 30.2, 124, and 27.8 μM, respectively. In other words, under normoxia and in the dark **Ru-STF31** was not much

more cytotoxic than **STF31**, which contributed to a higher PI value. The existence of synergies after light irradiation should hence not be over-interpreted in terms of molecular design, nor ignore that light-activated compounds should in principle maximize their photoindeX to offer low toxicity in the dark and high toxicity after activation.

Overall, targeting NAMPT inhibition for anticancer therapy showed a stunning lack of clinical success considering the link between NAMPT expression and tumor outcome. In other words, it has been difficult to find a good therapeutic window for such compounds. In our hands, the addition of NAD⁺ to hypoxic U87MG cells treated with free **STF31** demonstrated a reduction in the toxicity of the NAMPT inhibitor, supporting the idea that external NAD⁺ could moderate the adverse effects of NAMPT inhibition. These results suggested that the presence of extracellular NAD⁺ in the tumor microenvironment may rescue NAMPT inhibition and intracellular NAD⁺ depletion in the tumor cancer cells.^{51,52,43} In glioblastoma, extracellular NAD⁺ can be transported inside cells by membrane transporters named SLC (solute carrier family) or by gap junction with neighboring cells. Also, proteins such as connexin 43 hemichannels or CD38 may act as extracellular shuttles to transport NAD⁺.⁵³ Reduced efficacy of NAMPT inhibitors against tumors requires higher concentrations of the drug, which harms the patient. An unexpected outcome of our work emerged when combining red light-activated **Ru-STF31** with extracellular NAD⁺. Unlike the anticipated rescue effect, a toxicity increase was observed, as evidenced by a decrease in the EC₅₀ value of light-activated **Ru-STF31**. This unexpected interaction challenges the simplistic view of PACT compounds as simple light-activatable protein inhibitors and underscores the complex nature of cellular responses to treatments involving ruthenium photocages. More studies are needed to understand the reason(s) behind such interactions, and their consequence on antitumor efficacy of ruthenium-based PACT compounds *in vivo*, also as drug transporters, i.e., in absence of light activation. Overall, these observations highlight the complex interaction between oxygen concentration, NAD⁺ metabolism, and the cytotoxic mechanisms of **Ru-Py**, **Ru-STF31**, and free **STF31**. While oxygen concentration appears to significantly influence the cytotoxicity of **Ru-STF31** and free **STF31**, the role of NAMPT inhibition varied for the different compounds, and remained significant mostly under hypoxic conditions.

CONCLUSION

In conclusion, our study on the efficacy of the photoactivated NAMPT inhibitors **Ru-STF31** using U87MG cells as an *in vitro* tumor model, has provided valuable insights into the potential of ruthenium-based PACT treatment of high-grade gliomas. The correlation observed between NAMPT expression and glioma grading aligns with previous studies, highlighting the view that NAMPT plays a crucial role in glioma aggressiveness. Under hypoxic conditions, the upregulation of genes associated with the HIF1- α pathway in U87MG cells emphasizes their shared hypoxic features with real GBM tumors, confirming their appropriateness as *in vitro* experimental platform. The impact of **Ru-STF31** on high NAMPT-expressing U87MG cells, coupled with its unexpected interaction with NAD⁺, suggested new possibilities for using ruthenium compounds as hypoxia-targeted cancer therapies.

The drug- and O₂-concentration dependence of the biological interactions between the activated ruthenium photocage **RuOH₂** and the inhibitor **STF31** released by red light activation of **Ru-STF31**, underscores the potentially important biological effects of photoreleased ruthenium-based caging groups in Ru-based PACT. Our study demonstrates that it is possible to observe apparently opposing performance indicators for PACT compounds: clear-cut synergistic effects between the photoreleased inhibitor and cage, but a very low photoindeX due to the high

dark toxicity of the compound. It also highlights the importance of considering the tumor microenvironment and the O₂ status when studying combination therapies, at least for the treatment of glioblastoma. Additionally, the probable existence of off-targets suggests that ruthenium-based PACT complexes such as **Ru-STF31** might behave in a more complex fashion than as simple light-activatable protein inhibitors targeted “by design” to NAMPT. For example, the increased toxicity when combining NAD⁺ and **Ru-STF31** in the dark, highlighted the complex dynamics involved in the cellular responses to treatment with ruthenium complexes, which might explain the low photoindex of this PACT compound in particular under hypoxia. Overall, despite the mechanistic challenges revealed by this work, our findings provide valuable insights for refining NAMPT-targeted therapeutic strategies against glioblastoma. They urge for the development of new PACT compounds characterized by lower dark toxicity *and* synergistic action of the ruthenium-containing cage and the organic inhibitor, and this both under normoxia and hypoxia.

EXPERIMENTAL SECTION

Solvents and materials

Solvents used in the metabolomics study including acetonitrile and methanol in LC-MS grade and chloroform in HPLC grade were purchased from Biosolve BV (The Netherlands). MilliQ Ultra-pure water was obtained from a Merck Millipore A10 purification system (Raleigh, USA). Ammonium formate was purchased from Sigma-Aldrich (St. Louis, USA). The ¹³C,¹⁵N-labeled amino acids, and organic acids (U-¹³C₄, U-D₃, 9-¹⁵N-aspartate, U-¹³C₅-glutamine, 2,3,3-D₃-leucine, 1-¹³C, ¹⁵N-isoleucine, U-¹⁵N₂-UMP, ¹³C₃-pyruvate, 2,2,3,3-D₄-succinate, 2,2-D₂-glycine, 2,3-D₂-fumarate, U-¹³C₁₁, U-¹⁵N₂-tryptophan, U-¹³C₄, U-¹⁵N₂-asparagine, U-¹³C₅, U-D₅, ¹⁵N-glutamate, U-¹³C₅-valine, U-¹³C₆-lysine, ¹³C₃-lactate, 2,2,3,3-D₄-alanine) were purchased from Sigma-Aldrich and Cambridge Isotope Laboratories (Tewksbury, MA, USA).

The U87MG (Human primary Glioblastoma) cells were cultured in Dulbecco’s Modified Eagle Medium (DMEM) with 10% Fetal Calf Serum (FCS), 2 mM L-glutamine, and 0.2% Penstrep (100 mg/ml Penicillin + 100 mg/ml Streptomycin). The internal standard mix solution was prepared by mixing each standard stock solution (10 mM in milliQ water) and stored at -80 °C.

Cells were cultured in 25 or 75 cm² flasks under humidified conditions, at 37 °C, 5% CO₂, and 21% or 1% O₂ for normoxia or hypoxia, respectively. Upon reaching 70-80% confluence the cultures were split and cultured in a new flask.

Expression Data Retrieval from Human Protein Atlas

NAMPT expression in glioma patients and brain cancer cell lines assembled from the Human Protein Atlas (version 23.0), Ensemble (version 109).

Whole transcriptome analysis (TempO-Seq)

Targeted whole transcriptome analysis was performed using TempO-Seq (Yeakley et al., 2017). Three biological replications were made for each hypoxic and normoxic cell sample. Parallel samples were included for the Western blotting of the NAMPT protein. All cell lines were grown for 14 days in hypoxic (<1% O₂) normoxic (21% O₂) conditions in three different T75 cell culture flasks (Thermo Fisher Scientific, Cat.NO:156472). On day 14 cells were then seeded in a 96-well plate (Thermo Fisher Scientific, 10334513) with different densities, 50000, 80000, 40000, 60000, 100000 cells/ml for A549, A431, A375, U87MG and HepG2 (from ATCC) subsequently. Cells were then grown for 5 days under normoxia or hypoxia, and on day 19 the cells get lysed

by adding 1X TempO-seq Lysis buffer (20 μ L from BioSpyder Technologies Inc., Carlsbad, CA, USA) in each well. The cell lysate was stored at -80 $^{\circ}$ C and sent to the Biospyder company for TempO-Seq analysis. An R script developed in-house was used for count normalization and differential gene expression analysis. The minimum library size (total number of reads per sample) was set as 100,000 reads and samples below this size were removed. The CPM package⁵³ was used for count data normalization and to generate adjusted p-value (padj) and log2FoldChange values. Differentially expressed genes (DEGs) were selected by $|\log_2\text{Foldchange}| > 1$ and $\text{padj} < 0.05$ was used for making graphs using the GraphPad Prism 9.0.0 software.

Cell treatment and SRB cell viability assay

At $t = 0$ h, U87MG cells were seeded into 60 wells of 96-well plates (Thermo Fisher Scientific, 10334513) with a density of 60,000 cells/mL, with a seeding volume of 100 μ L leading to 6,000 cells/well. The outer walls were filled with 100 μ L PBS to avoid border effects. At $t = 24$ h the medium was refreshed, and the cells were treated with six different compounds concentrations. Cells at $t = 48$ h were irradiated at 630 nm for 45 min in Normoxia and 50min in Hypoxia to achieve light dose of 20.8J/cm² and plates without being treated by light were kept in dark. The end-point ($t = 96$ h), cell were fixed by adding cold trichloroacetic acid (10% w/v 100 μ L in each well) for performing SRB assay.⁵⁴ The plates were stored at 4 $^{\circ}$ C for 2 days, then the TCA medium mixture was removed, the cells were rinsed with demineralized water three times, and dried overnight. Then, each well was stained with 100 μ L S34 SRB solution (0.6% w/v SRB in 1% v/v acetic acid, sigma Aldrich, cas number:3520-42-1) for 30 min, the SRB solution was removed, and washed with acetic acid (1% v/v) for 3-5 times. Once the plates were dried overnight, 200 μ L of tris base (tromethamine, 10 mM, sigma aldrich, United states) was pipetted to each well. To determine the cell viability the absorbance at 510 nm was measured using a M1000 Tecan Reader. The SRB absorbance data per compound per concentration were interred to GraphPad Prism. The EC50 value calculated after removing background (absorbance of wells filled with PBS during treatment), concentrations (X) transformed to $\log(X)$. Two parametric hill slope evaluation with a fixed Y maximum (100%) and minimum (0%) relative cell population values was used to calculate EC₅₀ values.⁵⁵

$$Y = \frac{100}{(1 + 10^{((\log X - \log EC_{50}) \times Hill\ slope)})} \quad (3)$$

Combination Therapy

The Chou-Talalay method is a mathematical tool used to investigate the nature of drug interactions in combination therapy.⁵⁶ This method introduces the combination index value (CI) for quantifying synergism or antagonism for two drugs, calculated according to Equation (2). In combination treatment, **Ru-Py** (activated by RL, 630 nm, 20.8 J/cm²) and **STF31**, normoxic and hypoxic U87MG cells were seeded in 96 wells with the density of 80000 cells/mL. At $t = 24$ h, cells in column C-D-E were treated with **STF31** alone in 6 different concentrations (100-1.06 μ M), cells in column F-G-H-I-J-K were treated with **Ru-Py** alone in 6 different concentrations (100-1.06 μ M), and the cells were incubated further in the dark. At $t = 48$ h, cells were irradiated with red-light (630 nm, 20.8 J/cm²), corresponding to 42 min in normoxia (8,7 mW/cm²) and 51 min in hypoxia (5,8 mW/cm²). Immediately after irradiation, all cells were washed twice with drug-free medium, and **STF31** was added to the cells in columns I-J-K pretreated by **Ru-Py** (RL), with a 1:1 concentration ratio (100-1.06 μ M). The plates were incubated further in the dark. At $t = 96$ h, cells were fixed and an SRB assay for evaluating cell viability was performed. The SRB

absorbance in each condition were averaged over three identical technical replicates ($n = 3$) using Excel and imported in CompuSyn software, which generated the CompuSyn report including the combination index graphs shown in Figure 6.

For the NAD^+ combination treatment, all compounds were initially dissolved in DMSO, followed by dilution with PBS to a concentration of 1 mM of the compound with a maximum of 0.5% DMSO. The solution was further diluted with DMEM (Dulbecco Modified Eagle Medium) to achieve a 300 μM concentration of the compound. Cells were seeded at $t = 48$ h after cell seeding, the 96-well plates were irradiated with red light with a wavelength of 630 nm and light dose 20.8J/cm². The irradiated plates were maintained in a plate holder set at 37 °C, with irradiation lasting 50 min in hypoxia and 45 min in normoxia. Immediately post-irradiation, cells were treated with NAD^+ , which was dissolved in PBS to 2 mM and further diluted to working concentrations with the medium. At $t = 96$ h, i.e. 48 h after light activation, cells were fixed and SRB cell viability assay was used to quantify EC_{50} values.

Western blotting

All antibodies were provided by Cell Signaling, The Netherlands. 20 μg protein from the cell lines A375 (skin cancer), A549 (lung cancer), A431 (skin cancer), HEPG2 (liver cancer), and U87 (glioblastoma) cultured in normoxic and hypoxic conditions for 19 days were loaded on 4-15% polyacrylamide, mini-protein precast gels (Bio RAD, the Netherlands). The cells were provided by the American Type Culture Collection (ATCC) company. The running buffer consisted of 100 mL 10x tris-glycine buffer, 10 mL 10% SDS, 700 mL MiliQ water, and 200 mL methanol (MeOH). The gels were run for 5 min at 200 V and 1 h at 120 V. Subsequently, the proteins on the gels were transferred to the PVDF, (polyvinylidene difluoride) membrane by trans-blot turbo transfer system required by Bio-rad company (#1704150), the Netherlands. After the transfer of the proteins, the membranes were blocked with 5 mL of 5% milk in 0.1% TBS-Tween for 1 h at room temperature. Then, the membranes were incubated overnight with NAMPT antibody (3 mL 5% milk in 0.1% TBS-T (tris-buffered saline and Tween® 20) dilution: 1:1000, rabbit, mAb #86634) at 4 °C on the IKEA roller shaker, and incubated overnight. The membranes were washed 5 times for 3 min in TBS-T 0.1% and incubated with the secondary antibody anti-rabbit, #7074, (3 mL, TBS-T 0.1%, dilution is 1:1000) for 1 h at 24 °C. After incubation with the secondary antibody, the membranes were washed 5 times for 3 min with 0.1% TBS-T and were imaged by colorimetry and chemiluminescence with a Bio-rad ChemiDoc imaging System (#12003263). α -tubulin, 50 kDa, was used as the housekeeping gene. For blotting the housekeeping gene protein, the membranes were incubated with the α -tubulin primary antibody (mouse, 1:1000 in 3 mL 5% milk in 0.1% TBS-T) overnight at 4 °C on the roller bank. After incubation, the membranes were washed 5 times with 0.1% TBS-T and were incubated with the secondary antibody in 5% milk in 0.1% TBS-T (anti-rabbit, 1:1000) for 1 h at room temperature. The membranes were washed three times for 3 min in TBS-T 0.1% and were imaged by colorimetry and chemiluminescence with a Bio-rad imager.

Metabolomic study

U87MG cells cultured for 14 days in hypoxic or normoxic conditions were seeded in 6-well plates, with a density of 150,000 cells/well. In normoxic conditions, cells were treated with a 15 μM concentration for all compounds, which was intermediate between the $\text{EC}_{50,\text{RL}}$ value of Ru-Py (32.9 μM) and that of Ru-STF31 (9.7 μM). As in hypoxic cells we had observed resistance to our

treatment and the EC₅₀,RL value were almost twice higher than that in normoxic cells (22.7 and 9.72 μM for hypoxic and normoxic U87MG respectively), we treated cells with 30 μM of all compounds in such conditions. 72 h after light irradiation, (Red light wavelength of 630 nm and light dose 20.8J/cm²) for 45 min in normoxia and 50min in hypoxia) the cells were lysed and collected to probe the changes in NAD⁺ level using published metabolomics methods. For cell quenching and harvest, the medium was removed from all wells, and cells were washed with PBS and immediately quenched with cold 80% methanol. The content of each well was transferred into an Eppendorf tube and put into liquid nitrogen for fast freezing. All samples were later transferred to a -80 °C freezer for long-term storage before analysis.

For sample preparation, cell samples were lysed with sonication after one freeze–thaw cycle, vortexed, and then centrifuged at 16000g at 4 °C for 10 min. Cell pellets were collected to measure the protein content using a bicinchoninic acid assay (Cell Signaling, #7780). Supernatants were transferred into clean 1.5 mL Eppendorf tubes and evaporated to dryness in a Labconco SpeedVac (MO, United States). Each sample was reconstituted with 60 μL of ice-cold methanol/water (80%/20%; v/v). 50 μL of the reconstitution volume was collected and transferred into a new Eppendorf tube. The leftover volume was pooled together and aliquoted as quality control (QC) samples. 50 μL of cellular sample and QC samples were spiked with 5 μL of internal standard solution. A double liquid-liquid extraction (LLE) method was applied to treat samples by using mixed solvent chloroform/methanol/water (1/1/1, v/v/v). The upper aqueous phase was collected and evaporated to dryness⁴¹. The residue was reconstituted with 50 μL of ice-cold methanol/water (1/1, v/v). 3 μL of the final sample solution was used for LC-MS analysis. Metabolites including organic acids, amino acids, sugar phosphates, and nucleotides were measured on a HILIC-MS platform, which consisted of a SHIMAZU LC-30AD system with a SeQuant® ZIC-cHILIC HPLC Analytical PEEK Column (Merck) coupled to electrospray ionization on a triple time-of-flight mass spectrometer (AB SCIEX TripleTOF 5600). The mobile phases were composed of (A) 90% acetonitrile in H₂O with 5 mM ammonium formate and (B) 10 % acetonitrile in H₂O with 5 mM ammonium formate. Chromatographic separation of analytes was carried out with a gradient elution program at a flow rate of 0.5 mL/min^{40 41}. Electrospray ionization MS was operated in the negative ion mode and analytes were monitored in Time of Flight (ToF) mode at a full scan range of 50-900 m/z ^{40 41}. MultiQuant Software (AB SCIEX, Version 3.0.1) was used in the quantitative analysis for LC-MS raw data extraction and peak area integration. Internal standards were employed to correct random errors during sample preparation. Pooled QC samples were used to compensate for shifts in the sensitivity of the mass spectrometer over the batches based on the in-house developed algorithms, mzQuality³⁹. Corrected metabolite abundance was further normalized to the amount of protein in each sample. The Graphpad Prism software, version 9.0.0 was used for further analysis and for making graphs.

Acknowledgements

Dutch Research Council (NWO) is acknowledged for a VICI grant to S.B.

References

- (1) Ostrom, Q. T.; Cioffi, G.; Gittleman, H.; Patil, N.; Waite, K.; Kruchko, C.; Barnholtz-Sloan, J. S. CBTRUS Statistical Report: Primary Brain and Other Central Nervous System

Tumors Diagnosed in the United States in 2012–2016. *Neuro Oncol* **2019**, *21* (Suppl 5), v1–v100. <https://doi.org/10.1093/neuonc/noz150>.

(2) Chinot, O. L.; Wick, W.; Mason, W.; Henriksson, R.; Saran, F.; Nishikawa, R.; Carpentier, A. F.; Hoang-Xuan, K.; Kavan, P.; Cernea, D.; Brandes, A. A.; Hilton, M.; Abrey, L.; Cloughesy, T. Bevacizumab plus Radiotherapy–Temozolomide for Newly Diagnosed Glioblastoma. *N Engl J Med* **2014**, *370* (8), 709–722. <https://doi.org/10.1056/NEJMoa1308345>.

(3) Gilbert, M. R.; Wang, M.; Aldape, K. D.; Stupp, R.; Hegi, M. E.; Jaeckle, K. A.; Armstrong, T. S.; Wefel, J. S.; Won, M.; Blumenthal, D. T.; Mahajan, A.; Schultz, C. J.; Erridge, S.; Baumert, B.; Hopkins, K. I.; Tzuk-Shina, T.; Brown, P. D.; Chakravarti, A.; Curran, W. J.; Mehta, M. P. Dose-Dense Temozolomide for Newly Diagnosed Glioblastoma: A Randomized Phase III Clinical Trial. *J Clin Oncol* **2013**, *31* (32), 4085–4091. <https://doi.org/10.1200/JCO.2013.49.6968>.

(4) Gramatzki, D.; Dehler, S.; Rushing, E. J.; Zaugg, K.; Hofer, S.; Yonekawa, Y.; Bertalanffy, H.; Valavanis, A.; Korol, D.; Rohrmann, S.; Pless, M.; Oberle, J.; Roth, P.; Ohgaki, H.; Weller, M. Glioblastoma in the Canton of Zurich, Switzerland Revisited: 2005 to 2009. *Cancer* **2016**, *122* (14), 2206–2215. <https://doi.org/10.1002/cncr.30023>.

(5) Fernandez-Palomo, C.; Chang, S.; Prezado, Y. Should Peak Dose Be Used to Prescribe Spatially Fractionated Radiation Therapy?—A Review of Preclinical Studies. *Cancers (Basel)* **2022**, *14* (15), 3625. <https://doi.org/10.3390/cancers14153625>.

(6) Park, J. H.; Lee, H. K. Current Understanding of Hypoxia in Glioblastoma Multiforme and Its Response to Immunotherapy. *Cancers (Basel)* **2022**, *14* (5), 1176. <https://doi.org/10.3390/cancers14051176>.

(7) Cramer, S. W.; Chen, C. C. Photodynamic Therapy for the Treatment of Glioblastoma. *Front Surg* **2020**, *6*, 81. <https://doi.org/10.3389/fsurg.2019.00081>.

(8) Bhowmik, A.; Khan, R.; Ghosh, M. K. Blood Brain Barrier: A Challenge for Effectual Therapy of Brain Tumors. *Biomed Res Int* **2015**, *2015*, 320941. <https://doi.org/10.1155/2015/320941>.

(9) Aldape, K.; Brindle, K. M.; Chesler, L.; Chopra, R.; Gajjar, A.; Gilbert, M. R.; Gottardo, N.; Gutmann, D. H.; Hargrave, D.; Holland, E. C.; Jones, D. T. W.; Joyce, J. A.; Kearns, P.; Kieran, M. W.; Mellinghoff, I. K.; Merchant, M.; Pfister, S. M.; Pollard, S. M.; Ramaswamy, V.; Rich, J. N.; Robinson, G. W.; Rowitch, D. H.; Sampson, J. H.; Taylor, M. D.; Workman, P.; Gilbertson, R. J. Challenges to Curing Primary Brain Tumours. *Nat Rev Clin Oncol* **2019**, *16* (8), 509–520. <https://doi.org/10.1038/s41571-019-0177-5>.

(10) Dupont, C.; Mordon, S. R.; Deleporte, P.; Reyns, N.; Vermandel, M. A Novel Device for Intraoperative Photodynamic Therapy Dedicated to Glioblastoma Treatment. *Future Oncology* **2017**, Epub ahead of print. <https://doi.org/10.2217/fon-2017-0261>.

(11) Monro, S.; Colón, K. L.; Yin, H.; Roque, J. I.; Konda, P.; Gujar, S.; Thummel, R. P.; Lilge, L.; Cameron, C. G.; McFarland, S. A. Transition Metal Complexes and Photodynamic Therapy from a Tumor-Centered Approach: Challenges, Opportunities, and Highlights from the Development of TLD1433. *Chem. Rev.* **2019**, *119* (2), 797–828. <https://doi.org/10.1021/acs.chemrev.8b00211>.

(12) Foglar, M.; Aumiller, M.; Bochmann, K.; Buchner, A.; El Fahim, M.; Quach, S.; Sroka, R.; Stepp, H.; Thon, N.; Forbrig, R.; Rühm, A. Interstitial Photodynamic Therapy of Glioblastomas: A Long-Term Follow-up Analysis of Survival and Volumetric MRI Data. *Cancers (Basel)* **2023**, *15* (9), 2603. <https://doi.org/10.3390/cancers15092603>.

(13) Huang, Z.; Hsu, Y.-C.; Li, L.-B.; Wang, L.-W.; Song, X.-D.; Yow, C. M. N.; Lei, X.; Musani, A. I.; Luo, R.-C.; Day, B. J. Photodynamic Therapy of Cancer — Challenges of

- Multidrug Resistance. *J. Innov. Opt. Health Sci.* **2015**, *08* (01), 1530002. <https://doi.org/10.1142/S1793545815300025>.
- (14) Broekgaarden, M.; Weijer, R.; van Gulik, T. M.; Hamblin, M. R.; Heger, M. Tumor Cell Survival Pathways Activated by Photodynamic Therapy: A Molecular Basis for Pharmacological Inhibition Strategies. *Cancer Metastasis Rev* **2015**, *34* (4), 643–690. <https://doi.org/10.1007/s10555-015-9588-7>.
- (15) Shahmoradi Ghahe, S.; Kosicki, K.; Wojewódzka, M.; Majchrzak, B. A.; Fogtman, A.; Iwanicka-Nowicka, R.; Ciuba, A.; Koblowska, M.; Kruszewski, M.; Tudek, B.; Speina, E. Increased DNA Repair Capacity Augments Resistance of Glioblastoma Cells to Photodynamic Therapy. *DNA Repair* **2021**, *104*, 103136. <https://doi.org/10.1016/j.dnarep.2021.103136>.
- (16) Chen, Y.; Bai, L.; Zhang, P.; Zhao, H.; Zhou, Q. The Development of Ru(II)-Based Photoactivated Chemotherapy Agents. *Molecules* **2021**, *26*, 5679. <https://doi.org/10.3390/molecules26185679>.
- (17) Havrylyuk, D.; Hachey, A.; Glazer, E. Light-Activated Drugs for Photodynamic and Photoactivated Therapy. In *Targeted Metallo-Drugs*; CRC Press, 2023; pp 39–65.
- (18) Truong, V. X.; Barner-Kowollik, C. Photodynamic Covalent Bonds Regulated by Visible Light for Soft Matter Materials. *Trends in Chemistry* **2022**, *4* (4), 291–304. <https://doi.org/10.1016/j.trechm.2022.01.011>.
- (19) Cordones, A. A.; Lee, J. H.; Hong, K.; Cho, H.; Garg, K.; Boggio-Pasqua, M.; Rack, J. J.; Huse, N.; Schoenlein, R. W.; Kim, T. K. Transient Metal-Centered States Mediate Isomerization of a Photochromic Ruthenium-Sulfoxide Complex. *Nat Commun* **2018**, *9* (1), 1989. <https://doi.org/10.1038/s41467-018-04351-0>.
- (20) Lameijer, L. N.; Ernst, D.; Hopkins, S. L.; Meijer, M. S.; Askes, S. H. C.; Le Dévédec, S. E.; Bonnet, S. A Red-Light-Activated Ruthenium-Caged NAMPT Inhibitor Remains Phototoxic in Hypoxic Cancer Cells. *Angew Chem Int Ed Engl* **2017**, *56* (38), 11549–11553. <https://doi.org/10.1002/anie.201703890>.
- (21) van Rixel, V. H. S.; Ramu, V.; Auyeung, A. B.; Beztsinna, N.; Leger, D. Y.; Lameijer, L. N.; Hilt, S. T.; Le Dévédec, S. E.; Yildiz, T.; Betancourt, T.; Gildner, M. B.; Hudnall, T. W.; Sol, V.; Liagre, B.; Kornienko, A.; Bonnet, S. Photo-Uncaging of a Microtubule-Targeted Rigidin Analogue in Hypoxic Cancer Cells and in a Xenograft Mouse Model. *J. Am. Chem. Soc.* **2019**, *141* (46), 18444–18454. <https://doi.org/10.1021/jacs.9b07225>.
- (22) The potential of organometallic complexes in medicinal chemistry - ScienceDirect. <https://www.sciencedirect.com/science/article/pii/S1367593112000051> (accessed 2024-03-11).
- (23) Bretin, L.; Husiev, Y.; Ramu, V.; Zhang, L.; Hakkennes, M.; Abyar, S.; Johns, A. C.; Le Dévédec, S. E.; Betancourt, T.; Kornienko, A.; Bonnet, S. Red-Light Activation of a Microtubule Polymerization Inhibitor via Amide Functionalization of the Ruthenium Photocage. *Angewandte Chemie n/a (n/a)*, e202316425. <https://doi.org/10.1002/ange.202316425>.
- (24) Zhang, L.; Wang, P.; Zhou, X.-Q.; Bretin, L.; Zeng, X.; Husiev, Y.; Polanco, E. A.; Zhao, G.; Wijaya, L. S.; Biver, T.; Le Dévédec, S. E.; Sun, W.; Bonnet, S. Cyclic Ruthenium-Peptide Conjugates as Integrin-Targeting Phototherapeutic Prodrugs for the Treatment of Brain Tumors. *J Am Chem Soc* **2023**, *145* (27), 14963–14980. <https://doi.org/10.1021/jacs.3c04855>.
- (25) Tan, A.; Doig, C. L. NAD⁺ Degrading Enzymes, Evidence for Roles During Infection. *Front Mol Biosci* **2021**, *8*, 697359. <https://doi.org/10.3389/fmolb.2021.697359>.
- (26) Amjad, S.; Nisar, S.; Bhat, A. A.; Shah, A. R.; Frenneaux, M. P.; Fakhro, K.; Haris, M.; Reddy, R.; Patay, Z.; Baur, J.; Bagga, P. Role of NAD⁺ in Regulating Cellular and Metabolic Signaling Pathways. *Molecular Metabolism* **2021**, *49*, 101195. <https://doi.org/10.1016/j.molmet.2021.101195>.

- (27) Elhassan, Y. S.; Philp, A. A.; Lavery, G. G. Targeting NAD⁺ in Metabolic Disease: New Insights Into an Old Molecule. *J Endocr Soc* **2017**, *1* (7), 816–835. <https://doi.org/10.1210/js.2017-00092>.
- (28) Thongon, N.; Zucal, C.; D'Agostino, V. G.; Tebaldi, T.; Ravera, S.; Zamporlini, F.; Piacente, F.; Moschoi, R.; Raffaelli, N.; Quattrone, A.; Nencioni, A.; Peyron, J.-F.; Provenzani, A. Cancer Cell Metabolic Plasticity Allows Resistance to NAMPT Inhibition but Invariably Induces Dependence on LDHA. *Cancer Metab* **2018**, *6* (1), 1. <https://doi.org/10.1186/s40170-018-0174-7>.
- (29) Bordone, L.; Motta, M. C.; Picard, F.; Robinson, A.; Jhala, U. S.; Apfeld, J.; McDonagh, T.; Lemieux, M.; McBurney, M.; Szilvasi, A.; Easlon, E. J.; Lin, S.-J.; Guarente, L. Sirt1 Regulates Insulin Secretion by Repressing UCP2 in Pancreatic β Cells. *PLoS Biol* **2006**, *4* (2), e31. <https://doi.org/10.1371/journal.pbio.0040031>.
- (30) van der Horst, A.; Tertoolen, L. G. J.; de Vries-Smits, L. M. M.; Frye, R. A.; Medema, R. H.; Burgering, B. M. T. FOXO4 Is Acetylated upon Peroxide Stress and Deacetylated by the Longevity Protein hSir2(SIRT1). *J Biol Chem* **2004**, *279* (28), 28873–28879. <https://doi.org/10.1074/jbc.M401138200>.
- (31) Jieyu, H.; Chao, T.; Mengjun, L.; Shalong, W.; Xiaomei, G.; Jianfeng, L.; Zhihong, L. Nampt/Visfatin/PBEF: A Functionally Multi-Faceted Protein with a Pivotal Role in Malignant Tumors. *Current Pharmaceutical Design* **2012**, *18* (37), 6123–6132. <https://doi.org/10.2174/138161212803582531>.
- (32) Zhao, G.; Green, C.; Hui, Y.-H.; Prieto, L.; Shepard, R.; Dong, S.; Wang, T.; Tan, B.; Gong, X.; Kays, L.; Johnson, R.; Wu, W.; Bhattachar, S.; Prado, M.; Gillig, J.; Fernandez, M.-C.; Roth, K.; Buchanan, S.; Kuo, M.-S.; Burkholder, T. Discovery of a Highly Selective NAMPT Inhibitor That Demonstrates Robust Efficacy and Improved Retinal Toxicity with Nicotinic Acid Co-Administration. *Molecular cancer therapeutics* **2017**, *16*. <https://doi.org/10.1158/1535-7163.MCT-16-0674>.
- (33) Adams, D. J.; Ito, D.; Rees, M. G.; Seashore-Ludlow, B.; Puyang, X.; Ramos, A. H.; Cheah, J. H.; Clemons, P. A.; Warmuth, M.; Zhu, P.; Shamji, A. F.; Schreiber, S. L. NAMPT Is the Cellular Target of STF-31-like Small-Molecule Probes. *ACS Chem Biol* **2014**, *9* (10), 2247–2254. <https://doi.org/10.1021/cb500347p>.
- (34) Cuello-Garibo, J.-A.; Meijer, M. S.; Bonnet, S. To Cage or to Be Caged? The Cytotoxic Species in Ruthenium-Based Photoactivated Chemotherapy Is Not Always the Metal. *Chem. Commun.* **2017**, *53* (50), 6768–6771. <https://doi.org/10.1039/C7CC03469E>.
- (35) Azar, D. F.; Audi, H.; Farhat, S.; El-Sibai, M.; Abi-Habib, R. J.; Khnayzer, R. S. Phototoxicity of Strained Ru(II) Complexes. **2017**. <https://doi.org/10.1039/C7DT02255G>.
- (36) Wei, Y.; Xiang, H.; Zhang, W. Review of Various NAMPT Inhibitors for the Treatment of Cancer. *Front Pharmacol* **2022**, *13*, 970553. <https://doi.org/10.3389/fphar.2022.970553>.
- (37) Rana, N. K.; Singh, P.; Koch, B. CoCl₂ Simulated Hypoxia Induce Cell Proliferation and Alter the Expression Pattern of Hypoxia Associated Genes Involved in Angiogenesis and Apoptosis. *Biol Res* **2019**, *52*, 12. <https://doi.org/10.1186/s40659-019-0221-z>.
- (38) Chou, T.-C. Derivation and Properties of Michaelis-Menten Type and Hill Type Equations for Reference Ligands. *Journal of Theoretical Biology* **1976**, *59* (2), 253–276. [https://doi.org/10.1016/0022-5193\(76\)90169-7](https://doi.org/10.1016/0022-5193(76)90169-7).
- (39) Chou, T.-C. Theoretical Basis, Experimental Design, and Computerized Simulation of Synergism and Antagonism in Drug Combination Studies. *Pharmacol Rev* **2006**, *58* (3), 621–681. <https://doi.org/10.1124/pr.58.3.10>.
- (40) Huang, L.; Drouin, N.; Causon, J.; Wegrzyn, A.; Castro-Perez, J.; Fleming, R.; Harms, A.; Hankemeier, T. Reconstruction of Glutathione Metabolism in the Neuronal Model of Rotenone-

- Induced Neurodegeneration Using Mass Isotopologue Analysis with Hydrophilic Interaction Liquid Chromatography-Zeno High-Resolution Multiple Reaction Monitoring. *Anal. Chem.* **2023**, *95* (6), 3255–3266. <https://doi.org/10.1021/acs.analchem.2c04231>.
- (41) Hosseinkhani, F.; Huang, L.; Dubbelman, A.-C.; Guled, F.; Harms, A. C.; Hankemeier, T. Systematic Evaluation of HILIC Stationary Phases for Global Metabolomics of Human Plasma. *Metabolites* **2022**, *12* (2), 165. <https://doi.org/10.3390/metabo12020165>.
- (42) Vachher, M.; Arora, K.; Burman, A.; Kumar, B. NAMPT, GRN, and SERPINE1 Signature as Predictor of Disease Progression and Survival in Gliomas. *J Cell Biochem* **2020**, *121* (4), 3010–3023. <https://doi.org/10.1002/jcb.29560>.
- (43) Lucena-Cacace, A.; Otero-Albiol, D.; Jiménez-García, M. P.; Peinado-Serrano, J.; Carnero, A. NAMPT Overexpression Induces Cancer Stemness and Defines a Novel Tumor Signature for Glioma Prognosis. *Oncotarget* **2017**, *8* (59), 99514–99530. <https://doi.org/10.18632/oncotarget.20577>.
- (44) Lopez, J. S.; Banerji, U. Combine and Conquer: Challenges for Targeted Therapy Combinations in Early Phase Trials. *Nat Rev Clin Oncol* **2017**, *14* (1), 57–66. <https://doi.org/10.1038/nrclinonc.2016.96>.
- (45) Robey, I. F.; Lien, A. D.; Welsh, S. J.; Baggett, B. K.; Gillies, R. J. Hypoxia-Inducible Factor-1 α and the Glycolytic Phenotype in Tumors. *Neoplasia* **2005**, *7* (4), 324–330.
- (46) Lewis, J. E.; Singh, N.; Holmila, R. J.; Sumer, B. D.; Williams, N. S.; Furdui, C. M.; Kemp, M. L.; Boothman, D. A. Targeting NAD⁺ Metabolism to Enhance Radiation Therapy Responses. *Semin Radiat Oncol* **2019**, *29* (1), 6–15. <https://doi.org/10.1016/j.semradonc.2018.10.009>.
- (47) Smith, M. J.; Yang, F.; Griffiths, A.; Morrell, A.; Chapple, S. J.; Siow, R. C. M.; Stewart, T.; Maret, W.; Mann, G. E. Redox and Metal Profiles in Human Coronary Endothelial and Smooth Muscle Cells under Hyperoxia, Physiological Normoxia and Hypoxia: Effects of NRF2 Signaling on Intracellular Zinc. *Redox Biol* **2023**, *62*, 102712. <https://doi.org/10.1016/j.redox.2023.102712>.
- (48) Matsumoto, T.; Jimi, S.; Migita, K.; Takamatsu, Y.; Hara, S. Inhibition of Glucose Transporter 1 Induces Apoptosis and Sensitizes Multiple Myeloma Cells to Conventional Chemotherapeutic Agents. *Leuk Res* **2016**, *41*, 103–110. <https://doi.org/10.1016/j.leukres.2015.12.008>.
- (49) Ghanem, M. S. 1; Monacelli, F. 2; Nencioni, A. 2 1 D. of I. M.; Medical Specialties (DIMI), U. of G.; Moustafa.Ghanem@edu.unige.it (M.S.G.); Medicine, fiammetta monacelli@unige.it (F.M.) 2 D. of I.; Medical Specialties (DIMI), U. of G.; Moustafa.Ghanem@edu.unige.it (M.S.G.); fiammetta.monacelli@unige.it (F.M.); Ospedale Policlinico San Martino IRCCS, L. R. B. 10. Advances in NAD-Lowering Agents for Cancer Treatment. **2021**, 1665. <https://doi.org/10.3390/nu13051665>.
- (50) Guda, M. R.; Labak, C. M.; Omar, S. I.; Asuthkar, S.; Airala, S.; Tuszynski, J.; Tsung, A. J.; Velpula, K. K. GLUT1 and TUBB4 in Glioblastoma Could Be Efficacious Targets. *Cancers (Basel)* **2019**, *11* (9), 1308. <https://doi.org/10.3390/cancers11091308>.
- (51) Billington, R. A.; Genazzani, A. A.; Travelli, C.; Condorelli, F. NAD Depletion by FK866 Induces Autophagy. *Autophagy* **2008**, *4* (3), 385–387. <https://doi.org/10.4161/auto.5635>.
- (52) Lucena-Cacace, A.; Otero-Albiol, D.; Jiménez-García, M. P.; Muñoz-Galvan, S.; Carnero, A. NAMPT Is a Potent Oncogene in Colon Cancer Progression That Modulates Cancer Stem Cell Properties and Resistance to Therapy through Sirt1 and PARP. *Clinical Cancer Research* **2018**, *24* (5), 1202–1215. <https://doi.org/10.1158/1078-0432.CCR-17-2575>.

- (53) Ross, G. J. Parametric and Nonparametric Sequential Change Detection in R: The Cpm Package. *Journal of Statistical Software* **2015**, *66*, 1–20. <https://doi.org/10.18637/jss.v066.i03>.
- (54) Vichai, V.; Kirtikara, K. Sulforhodamine B Colorimetric Assay for Cytotoxicity Screening. *Nat Protoc* **2006**, *1* (3), 1112–1116. <https://doi.org/10.1038/nprot.2006.179>.
- (55) Hopkins, S. L.; Siewert, B.; Askes, S. H. C.; Veldhuizen, P.; Zwier, R.; Heger, M.; Bonnet, S. An in Vitro Cell Irradiation Protocol for Testing Photopharmaceuticals and the Effect of Blue, Green, and Red Light on Human Cancer Cell Lines. *Photochem Photobiol Sci* **2016**, *15* (5), 644–653. <https://doi.org/10.1039/c5pp00424a>.
- (56) Zhang, N.; Fu, J.-N.; Chou, T.-C. Synergistic Combination of Microtubule Targeting Anticancer Fludelone with Cytoprotective Panaxytriol Derived from Panax Ginseng against MX-1 Cells in Vitro: Experimental Design and Data Analysis Using the Combination Index Method. *Am J Cancer Res* **2015**, *6* (1), 97–104.